Lensing magnification: implications for counts of submillimetre galaxies and SZ clusters

Marcos Lima,[★] Bhuvnesh Jain and Mark Devlin

Department of Physics and Astronomy, University of Pennsylvania, Philadelphia, PA 19104, USA

ABSTRACT

We study lensing magnification of source galaxies by intervening galaxy groups and clusters using a halo model. Haloes are modelled with truncated NFW profiles with ellipticity added to their lensing potential and propagated to observable lensing statistics. We present the formalism to calculate observable effects due to a distribution of haloes of different masses at different redshifts along the line of sight. We calculate the effects of magnification on the number counts of high-redshift galaxies. Using Balloon-borne Large Aperture Submillimetre Telescope (BLAST) survey data for submillimetre galaxies (SMGs), we find that magnification affects the steep, high flux part of the counts by about 60 per cent. The effect becomes much stronger if the intrinsic distribution is significantly steeper than observed. We also consider the effect of this high-redshift galaxy population on contaminating the Sunyaev–Zel'dovich (SZ) signal of massive clusters using the halo model approach. We find that for the majority of clusters expected to be detected with ongoing SZ surveys, there is significant contamination from the Poisson noise due to background SMGs. This contribution can be comparable to the SZ increment for typical clusters and can also contaminate the SZ decrement of low-mass clusters. Thus, SZ observations, especially for the increment part of the SZ spectrum, need to include careful modelling of this irreducible contamination for mass estimation. Lensing further enhances the contamination, especially close to the cores of massive clusters and for very disturbed clusters with large magnification cross-section.

Key words: gravitational lensing: strong – galaxies: clusters: general – cosmology: observations – submillimetre: galaxies.

1 INTRODUCTION

Gravitational lensing, the deflection of light rays from background galaxies by intervening objects, has a number of cosmological and astrophysical applications (Schneider, Ehlers & Falco 1992; Blandford & Narayan 1992; Narayan & Bartelmann 1996; Bartelmann & Schneider 2001; Schneider, Kochanek & Wambsganss 2006; Hoekstra & Jain 2008). In the weak lensing regime, small distortions of source galaxies can statistically constrain cosmological parameters related to structure formation and theories of gravity. In the strong lensing regime, where light is deflected by rare massive galaxy clusters, it is also possible to infer detailed information on cluster profiles, though with less statistics. Although lensing conserves surface brightness of sources, it changes their observed fluxes and sizes; e.g. background galaxies have their fluxes magnified in the line-of-sight of massive haloes cores.

Galaxy clusters that produce dramatic lensing effects are themselves potentially powerful cosmological probes (Wang & Steinhardt 1998; Haiman, Mohr & Holder 2001), provided one can detect them in pure samples, and measure their masses and redshifts precisely (Hu 2003; Lima & Hu 2005, 2007; Rozo et al. 2007, 2010). Techniques for cluster detection and mass measurement include the counting of optical galaxies, the measurement of their lensing signal, their X-ray temperature or flux and their Sunyaev–Zel'dovich (SZ) flux decrement/increment (SZ effect). The SZ effect (Sunyaev & Zeldovich 1972; Itoh, Kohyama & Nozawa 1998; Birkinshaw 1999; Carlstrom, Holder & Reese 2002) results from the up-scatter of cosmic microwave background (CMB) photons by the hot electrons in the intra-cluster medium, which shifts the underlying spectrum and causes a decrement/increment at wavelengths longer/shorter than ∼1 mm. This allows for the detection of clusters independently of their redshifts and the measurement of their masses, as long as the effects of possible contaminants, such as radio sources and far-IR/submillimetre galaxies (SMGs) can be removed or at least well understood.

[★]E-mail: mlima@sas.upenn.edu

The SMG population consists of dusty high-redshift galaxies with high star formation rates (Blain & Longair 1993; Barger et al. 1998; Hughes et al. 1998; Blain et al. 2002). The energy output of the star-forming regions heats up dust grains, which emit a modified blackbody spectrum that peaks around 0.1 mm in the rest frame. SMGs can produce a non-negligible point-source contribution to CMB anisotropies (Scott & White 1999). When positioned on the line-of-sight of cluster cores, these galaxies can contaminate the cluster SZ flux, filling up the decrement and enhancing the increment, resulting in misestimation of the cluster mass from SZ measurements (Knox, Holder & Church 2004; White & Majumdar 2004). In addition, galaxy clusters can magnify the fluxes of the SMGs (Blain 1996, 1997, 1999; Paciga, Scott & Chapin 2009), changing their counts distribution and further enhancing the contamination of the SZ signal.

In this paper, we study the effect of lensing magnification of SMGs by foreground clusters from a twofold perspective. On the one hand, galaxy clusters magnify the fluxes of SMGs, changing their intrinsic counts distribution, but potentially facilitating their detection and follow-up studies. On the other hand, the magnified fluxes of SMGs can contaminate unresolved SZ clusters and may need to be understood in order to provide clean SZ mass estimates. For instance, Diego & Partridge (2009) find that including point sources in the modelling of cluster masses results in better agreement between X-ray and SZ mass estimates. Follow-up observations of unresolved clusters provide a means to tackle these issues, allowing for separation and removal of SZ contaminants and detailed studies of their properties.

We start in Section 2 by describing the properties of the dark matter haloes used to represent the lens galaxy clusters. In Section 3, we briefly review the basic formalism to analytically compute lensing magnification by massive haloes, and in Section 4 we describe the lensing probability and some of its applications. Our main results are shown in Section 5, where we estimate the effects of lensing on the SMGs distributions (Section 5.1) and show the contamination effect of the (lensed) SMG population on the SZ flux of clusters (Section 5.2). We conclude in Section 6.

Throughout, we assume a fiducial cosmology for a flat universe with parameter values based on the results of the *Wilkinson Microwave Anisotropy Probe* first year data release (*WMAP*1) (Spergel et al. 2003). The cosmological parameters (and their values) are the normalization of the initial curvature spectrum $\delta_\zeta (=5.07 \times 10^{-5})$ at $k = 0.05$ Mpc^{-1} (corresponding to $\sigma_8 = 0.91$), its tilt $n (=1)$, the baryon density relative to critical $\Omega_b h^2 (=0.024)$, the matter density $\Omega_m h^2 (=0.14)$ and two dark energy parameters: its density $\Omega_{DE} (=0.73)$ and equation of state $w (=-1)$, which we assume to be constant.

2 HALO PROPERTIES

In this section we present the halo properties and scaling relations assumed throughout to estimate lensing effects of galaxy clusters. We take the NFW profile prescription for dark matter haloes (Navarro, Frenk & White 1997)

$$\rho(r) = \frac{\rho_s}{(cr/r_{vir})(1 + cr/r_{vir})^2} \, , \tag{1}$$

where r_{vir} is the virial radius and the halo concentration c is given by a fit to simulations from Bullock et al. (2001)

$$c(M_{vir}, z) = \frac{9}{1+z} \left(\frac{M_{vir}}{M_*} \right)^{-0.13} \, , \tag{2}$$

with M_* such that $\sigma(M_*) = \delta_c$. Here, $\sigma^2(M)$ is the variance of the linear density field, defined in equation (9), and δ_c is the linearly extrapolated density contrast threshold in spherical collapse. Even though δ_c has a small redshift and cosmology dependency, here we take it to be fixed at its value in a $\Omega_m = 1$ universe, i.e. $\delta_c = 1.686$. The halo virial mass M_{vir} is

$$M_{vir} = \int_0^{r_{vir}} dr 4\pi r^2 \rho(r) = \frac{4\pi \rho_s r_{vir}^3}{c^3} f^{-1} \, , \tag{3}$$

where $f = (\ln(1+c) - c/(1+c))^{-1}$. The virial radius r_{vir} can be computed from the virial overdensity Δ_c relative to *critical* density

$$\Delta_c = \frac{3M_{vir}}{\rho_{crit}(z) 4\pi r_{vir}^3} \, , \tag{4}$$

where $\rho_{crit}(z) = \rho_{crit,0} E^2(z)$ is the critical density at redshift z, $\rho_{crit,0}$ is its value at $z = 0$ and the scaled Hubble parameter is

$$E^2(z) = \frac{H^2(z)}{H_0^2} = \Omega_m (1+z)^3 + \Omega_{DE}(1+z)^{3(1+w)} \, . \tag{5}$$

We take Δ_c from a fit to simulations of Bryan & Norman (1998) for flat cosmologies

$$\Delta_c = 18\pi^2 + 82x - 39x^2 \, , \tag{6}$$

where $x = \omega_m(z) - 1$ and $\omega_m(z) = \Omega_m(1+z)^3/E^2(z)$. One can similarly define the overdensity relative to the *mean matter* density $\Delta_{vir} = \Delta_c/\omega_m(z)$. Finally, for the halo distribution in mass and redshift we take the description of Sheth & Tormen (1999) for the *comoving* differential number density of haloes per logarithmic mass interval

$$\frac{dn}{d\ln M_{vir}} = \frac{\bar{\rho}_m}{M_{vir}} f(\nu) \frac{d\nu}{d\ln M_{vir}} \, , \tag{7}$$

where $\nu = \delta_c/\sigma(M_{vir})$ and

$$\nu f(\nu) = A\sqrt{\frac{2}{\pi} a\nu^2} [1 + (a\nu^2)^{-p}] \exp[-a\nu^2/2] \, . \tag{8}$$

Here $\sigma^2(M)$ is the variance of the linear density field in a top hat of radius r that encloses $M = 4\pi r^3 \bar{\rho}_m/3$ at the background density

$$\sigma^2(r) = \int \frac{d^3k}{(2\pi)^3} |\tilde{W}(kr)|^2 P_L(k), \tag{9}$$

where $P_L(k)$ is the linear power spectrum and $\tilde{W}$ is the Fourier transform of the top hat window. The normalization constant A is such that $\int d\nu f(\nu) = 1$ and we take the parameter values $p = 0.3, a = 0.75$.

3 LENSING MAGNIFICATION BY MASSIVE HALOES

3.1 Axially symmetric lenses

Given the 3D density profile $\rho(r)$, we can compute all lensing quantities of interest in the lens plane by performing successive numerical integrations and differentiations. For the NFW profile, most quantities can be computed analytically, speeding up calculations that use the lensing properties. The projected density field Σ is obtained integrating over the parallel coordinate $r_\parallel = \chi$ in the position vector decomposed as $\boldsymbol{x} = (r_\parallel, r_\perp)$, where the perpendicular coordinate $r_\perp = D_A(\chi)\theta$, D_A is the angular diameter distance and θ is the angular coordinate in the lens plane. Here and throughout, all distances are *comoving*. For the NFW profile the projected surface density is given by (Takada & Jain 2003a)

$$\Sigma(\theta) = \int_{-r_{\rm vir}}^{r_{\rm vir}} dr_\parallel \rho(r) = \frac{M_{\rm vir} f c^2}{2\pi r_{\rm vir}^2} F(c\theta/\theta_{\rm vir}), \tag{10}$$

where

$$F(x) = \begin{cases} -\frac{\sqrt{c^2-x^2}}{(1-x^2)(1+c)} + \frac{1}{(1-x^2)^{3/2}} \operatorname{arccosh} \frac{x^2+c}{x(1+c)}, & (x < 1) \\ \frac{\sqrt{c^2-1}}{3(1+c)} \left[1 + \frac{1}{c+1}\right], & (x = 1) \\ -\frac{\sqrt{c^2-x^2}}{(1-x^2)(1+c)} - \frac{1}{(x^2-1)^{3/2}} \arccos \frac{x^2+c}{x(1+c)}, & (1 < x < c) \\ 0, & (x > c) \end{cases} \tag{11}$$

and $\theta_{\rm vir}(\chi) = r_{\rm vir}/D_A(\chi)$. The convergence field κ is defined in terms of the critical density $\Sigma_{\rm crit}$ by

$$\kappa(\theta) = \frac{\Sigma(\theta)}{\Sigma_{\rm crit}}, \quad \Sigma_{\rm crit} = \frac{a}{4\pi G} \frac{D_A(\chi_s)}{D_A(\chi)D_A(\chi_s - \chi)}. \tag{12}$$

where $a = (1+z)^{-1}$ is the scalefactor. The convergence measures isotropic light distortions and is related to the projected lensing potential φ via the Poisson equation $\nabla^2 \varphi = 2\kappa$. Anisotropic distortions are measured by the complex shear field $\boldsymbol{\gamma} = \gamma_1 + i\gamma_2$, whose amplitude for an *axially symmetric* mass distribution is simply related to the convergence by

$$\gamma(\theta) = \bar{\kappa}(<\theta) - \kappa(\theta), \tag{13}$$

where the average convergence field up to θ is

$$\bar{\kappa}(<\theta) = \frac{1}{\pi\theta^2} \int_0^\theta d\theta' 2\pi\theta' \kappa(\theta'). \tag{14}$$

Like the convergence, the shear can be computed analytically for the NFW profile and is given by (Takada & Jain 2003b)

$$\gamma(\theta) = \frac{M_{\rm vir} f c^2}{2\pi r_{\rm vir}^2} \frac{G(c\theta/\theta_{\rm vir})}{\Sigma_{\rm crit}}, \tag{15}$$

where

$$G(x) = \begin{cases} \frac{1}{x^2(1+c)} \left[\frac{(2-x^2)\sqrt{c^2-x^2}}{1-x^2} - 2c\right] + \frac{2}{x^2} \ln \frac{x(1+c)}{c+\sqrt{c^2-x^2}} + \frac{2-3x^2}{x^2(1-x^2)^{3/2}} \operatorname{arccosh} \frac{x^2+c}{x(1+c)}, & (x < 1) \\ \frac{1}{3(1+c)} \left[\frac{(11c+10)\sqrt{c^2-1}}{1+c} - 6c\right] + 2\ln \frac{1+c}{c+\sqrt{c^2-1}}, & (x = 1) \\ \frac{1}{x^2(1+c)} \left[\frac{(2-x^2)\sqrt{c^2-x^2}}{(1-x^2)} - 2c\right] + \frac{2}{x^2} \ln \frac{x(1+c)}{c+\sqrt{c^2-x^2}} - \frac{2-3x^2}{x^2(x^2-1)^{3/2}} \arccos \frac{x^2+c}{x(1+c)}, & (1 < x < c). \\ \frac{2f^{-1}}{x^2}. & (x > c) \end{cases} \tag{16}$$

Finally, the magnification μ measures the total flux amplification as well as the increase in angular size of source galaxies, and is given by the inverse determinant of the Jacobian transformation between source and image angular coordinates. It is expressed in terms of the convergence and shear as

$$\mu(\theta) = \frac{1}{[1 - \kappa(\theta)]^2 - |\gamma(\theta)|^2}. \tag{17}$$

In Fig. 1, we show various lensing observables, assuming a spherical NFW profile lens halo of mass $M_{\rm vir} = 10^{14} \, h^{-1} \, {\rm M}_\odot$ at redshift $z_l = 0.2$ and a source galaxy at $z_s = 1.0$. The convergence tends to dominate over the shear in the halo core whereas the shear dominates in the
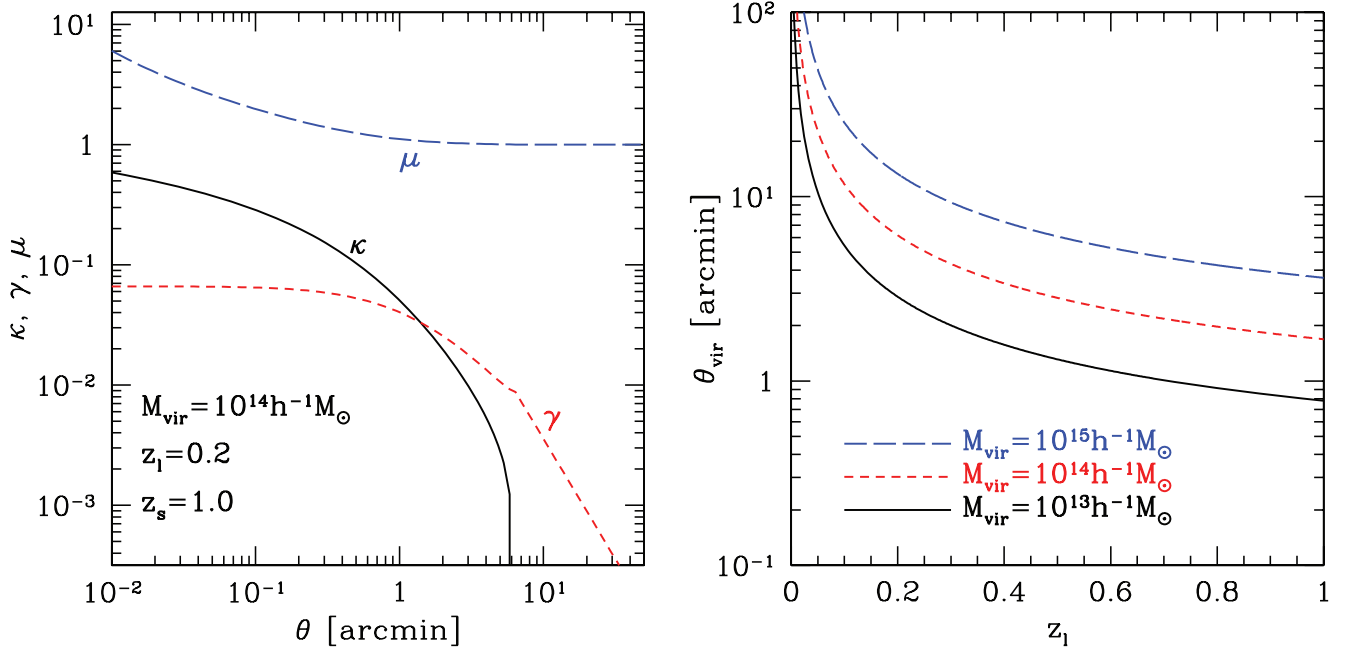
Figure 1. Left: convergence κ, shear γ and magnification μ as a function of angular separation θ from the halo centre. Here the lens mass and redshift are $M_{\rm vir} = 10^{14}\, h^{-1}\, \rm M_\odot$ and $z_{\rm l} = 0.2$, the source is at redshift $z_{\rm s} = 1.0$ and the halo is assumed to have a NFW profile. Right: the virial radius $\theta_{\rm vir}$ in angular units as a function of $z_{\rm l}$ for different halo masses.

outer parts. Likewise, the magnification is close to 1 (no magnification) far from the halo and rises to significant values close to the cluster centre. Also shown is the virial radius in angular units $\theta_{\rm vir}$ as a function of halo redshift for different halo masses. Haloes of interest have typical angular sizes of the order of a few arcmin.

In Fig. 2, we show the magnification μ as a function of angular separation θ, lens redshift $z_{\rm l}$ and source redshift $z_{\rm s}$ for different cluster masses. As the halo mass increases the magnification is significantly enhanced. The two spikes in each magnification curve at the top panels of Fig. 2 represent critical curves (tangential and radial) where the magnification is formally infinite and corresponds to the two solutions of the quadratic equation $|1 - \kappa|^2 = \gamma^2$.

Magnification increases with lens redshift, reaching a maximum and then decreases as the lens approaches the source; that reflects the lensing efficiency of the critical surface density terms. Magnification also increases with source redshift, until it reaches a plateau; therefore one expects roughly similar lensing magnification effects from sources at sufficiently high redshifts.

In what follows, we use the letters κ, γ and μ to denote *full* lensing quantities, which incorporate halo ellipticity (Section 3.2). The spherically symmetric results of this section will be denoted by the same letters with a tilde (e.g. $\tilde{\kappa}$).

3.2 Elliptical lenses

Ellipticity can be introduced in a number of ways into halo profiles. The most obvious choice is to introduce it directly into the 3D density profile $\rho(r)$ and project it to obtain Σ. Another choice is to introduce ellipticity in Σ directly. The computation of the lensing quantities can then be obtained numerically by performing integrations (of Σ) to obtain deflection angles, and differentiations (of deflection angles) to obtain shear and magnification fields. In special cases of known potential-density pairs, these quantities can be computed analytically.

Another possibility is to introduce ellipticity in the two-dimensional projected lensing potential φ, whose second derivatives give the lensing quantities more directly. The latter approach may produce density profiles with dumbbell shapes for high values of ellipticity, but produces physical magnification fields for low/intermediate ellipticities close to those expected for the majority of haloes (Jing & Suto 2002). Moreover, this approach leads to simple analytical expressions that can be expressed in terms of the usual results of the spherically symmetrical case and, for this reason, this is the choice we implement.

3.2.1 Elliptical potential

Given an axially symmetric lensing potential $\varphi(\theta)$, we follow Meneghetti, Bartelmann & Moscardini (2003) and obtain the elliptical generalization with major axis along the θ_2-direction by substituting $\theta^2 = \theta_1^2 + \theta_2^2$ by

$$\theta \to \bar{\theta} = \sqrt{\frac{\theta_1^2}{(1 - e_\varphi)} + \theta_2^2 (1 - e_\varphi)}, \tag{18}$$
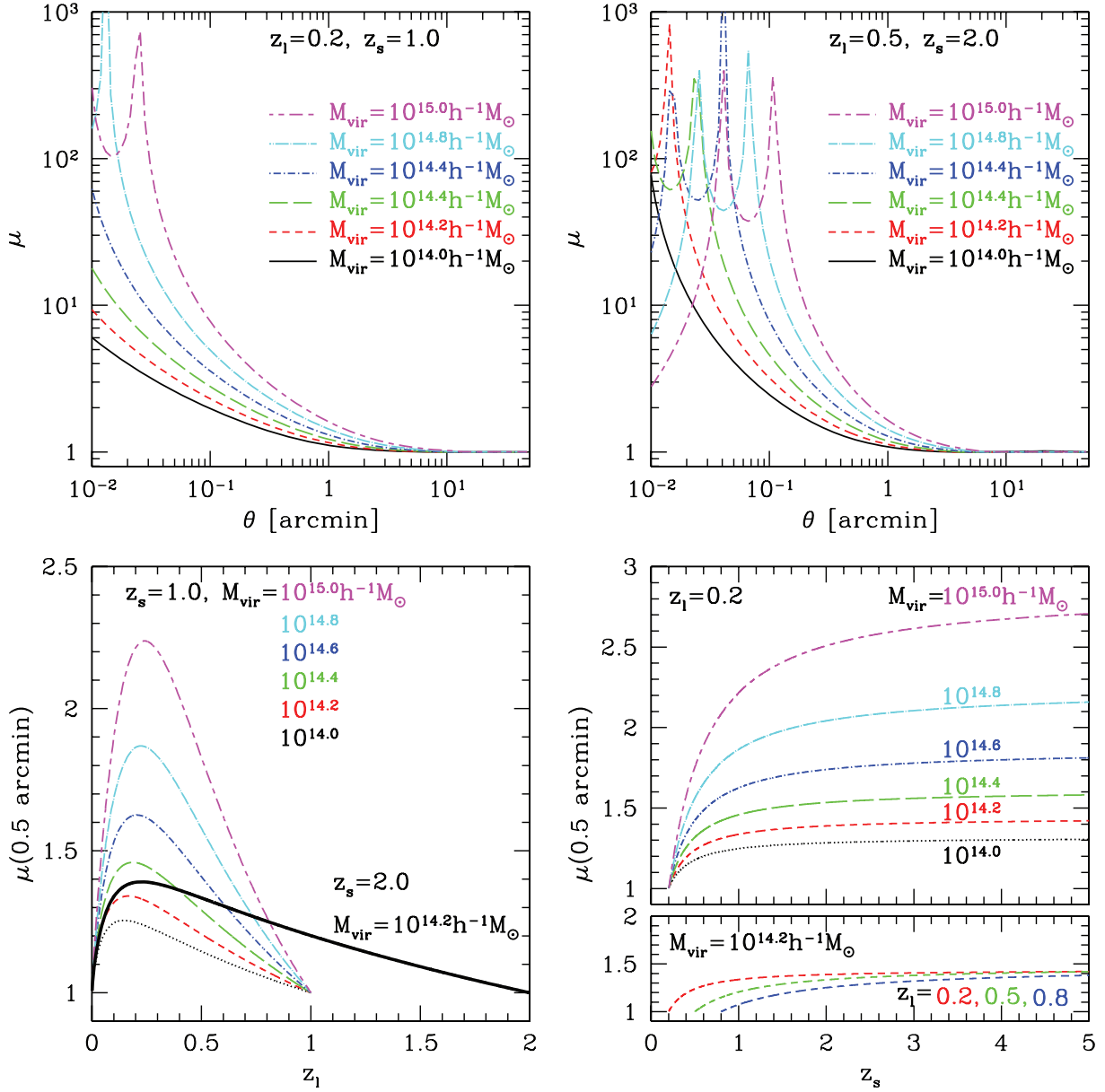
Figure 2. Top left: magnification μ as a function of angular separation θ from the cluster centre, assuming an NFW profile, for different cluster masses with $z_l = 0.2$ and $z_s = 1.0$. Top right: same but for $z_l = 0.5$ and $z_s = 2.0$. Bottom left: μ evaluated at $\theta = 0.5$ arcmin as a function of lens redshift z_l for $z_s = 1.0$ at different cluster masses and for $z_s = 2.0$ for cluster mass $M_{\mathrm{vir}} = 10^{14.2} \, h^{-1} \, \mathrm{M}_\odot$. Bottom right: $\mu(\theta = 0.5$ arcmin) as a function of source redshift z_s for $z_l = 0.2$ at different cluster masses (upper panel) and for $M_{\mathrm{vir}} = 10^{14.2} \, h^{-1} \, \mathrm{M}_\odot$ at different values of z_l (lower panel).

where $e_\varphi = 1 - b/a$ with a and b being the major and minor ellipse axes. Our approach is similar to that of Golse & Kneib (2002), though our NFW profiles are truncated at the virial radius as opposed to extending to infinity. We can then compute the deflection angle components, their derivatives and the lensing quantities of interest for elliptical lenses. In Appendix A, we express the results for κ, γ_1 and γ_2 in terms of the spherically symmetric case, with the effects of ellipticity described analytically. Using the expressions given in equations (A11), (A12) and (A13) we can compute the magnification defined by equation (17).

In Fig. 3, we show magnification maps in the $\theta_1 \times \theta_2$ plane, for different ellipticities. The top row shows maps derived using our model in which ellipticity is introduced in the lensing potential. The bottom row shows maps derived using the WSLAP code (Diego et al. 2007), where ellipticity e_κ is introduced in the 3D density profile, which is then projected. Note that both agree when $e_\varphi = e_\kappa = 0$ and that the ellipticity introduced in the potential causes larger changes in the magnification map. This is expected, since the second derivative of the potential is related to the density – the quantitative connection between the two is presented below.

In Fig. 4, we show the magnification μ as a function of angular separation along the two directions θ_1 and θ_2 for different values of e_φ. In the θ_2-direction of the major axis, the tangential caustic moves to larger angles whereas the radial caustic moves to smaller angles. In the θ_1-direction much less dramatic changes happen, as also seen in Fig. 3.
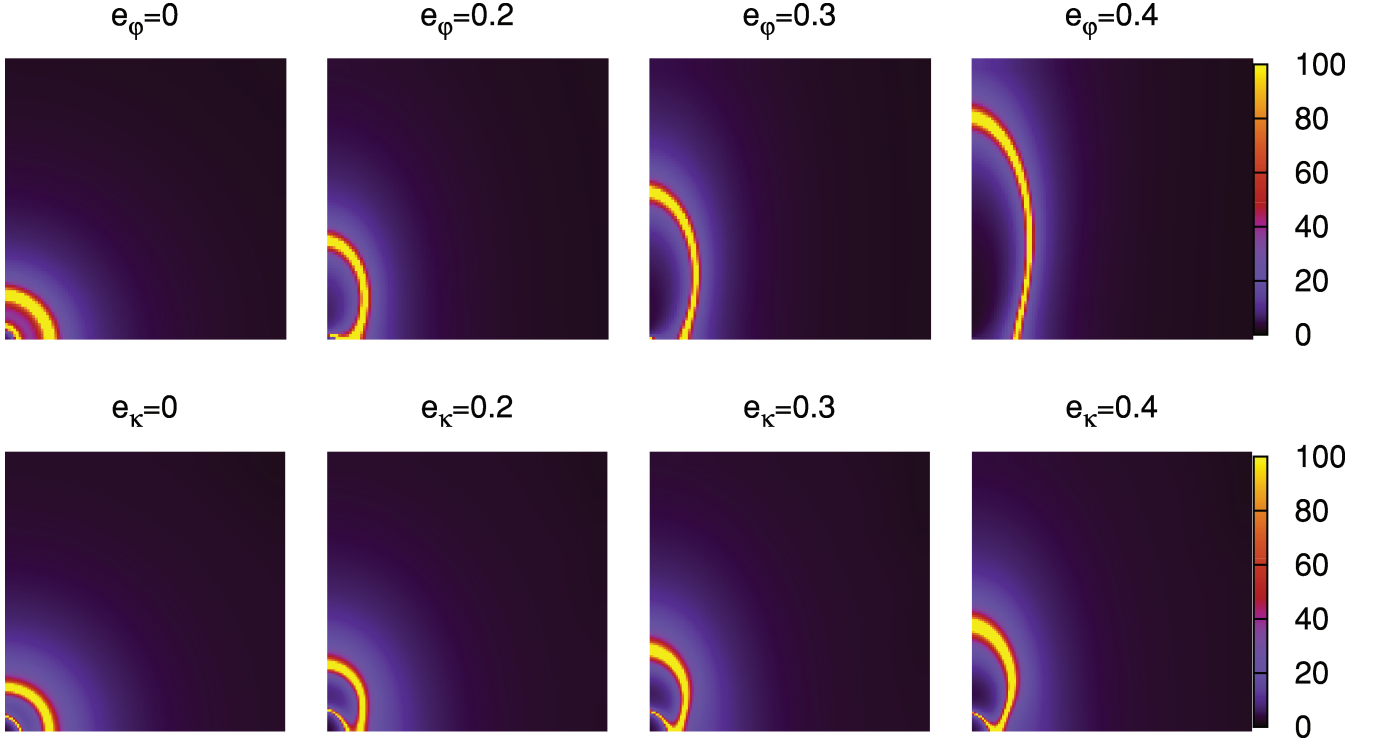
Figure 3. Maps of magnification μ for different values of ellipticity with $z_l = 0.5$ and $z_s = 2.0$ and halo mass $M_{vir} = 10^{15} \, h^{-1} \, M_\odot$. Here, $e = 1 - b/a$, where a and b are the projected major and minor ellipse axes in the lens plane. Top panels: ellipticity e_φ is introduced directly in the *potential* profile using the analytical expressions derived in this paper. Bottom panels: ellipticity e_κ is introduced in the *density* profile and propagated to the deflection angle and magnification numerically using the WSLAP code of Diego et al. (2007). Notice that $e_\varphi = 0.2$ produces roughly the same magnification map as $e_\kappa = 0.4$. The field of view is 0.6 arcmin in size.
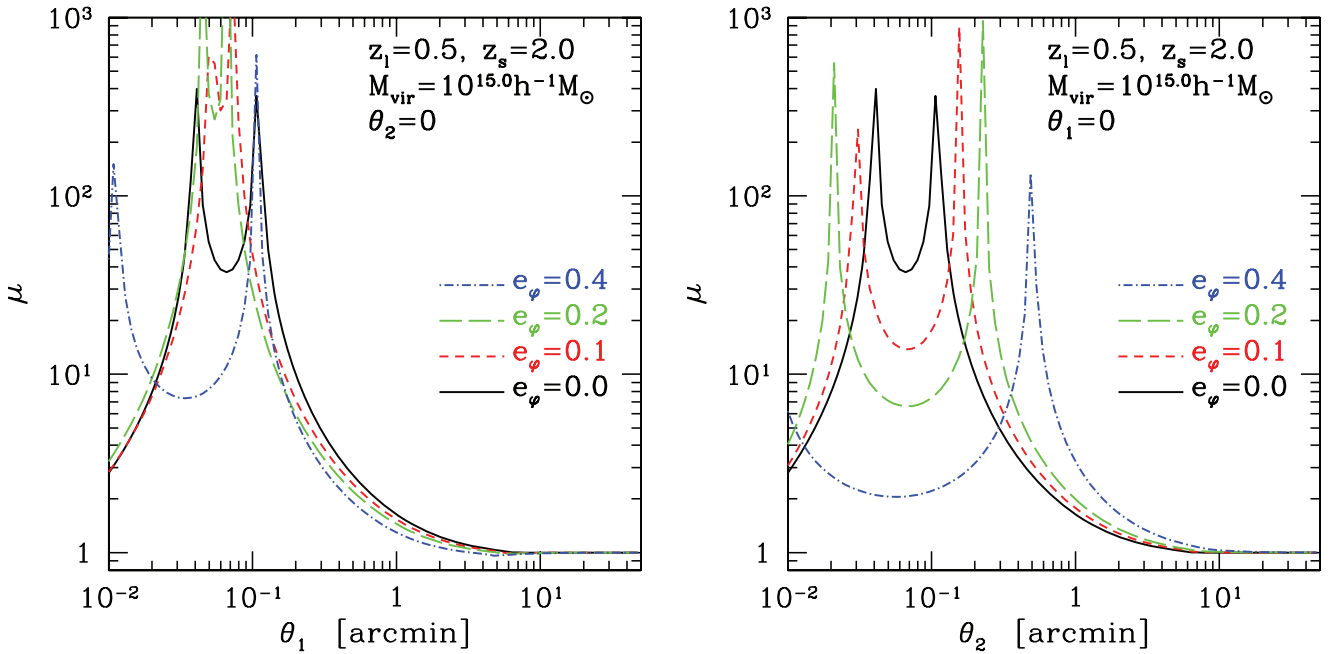

Figure 4. Left: magnification μ as a function of angular separation from the cluster centre in the θ_1-direction ($\theta_2 = 0$). Right: same but in the θ_2-direction ($\theta_1 = 0$). We assume an elliptical NFW profile, with different values of ellipticity, $z_l = 0.5$ and $z_s = 2.0$. Here, $e_\varphi = 1 - b/a$, where a and b are the major and minor ellipse axes and ellipticity is introduced in the lensing potential in the θ_2-direction with the prescription of Meneghetti et al. (2003).
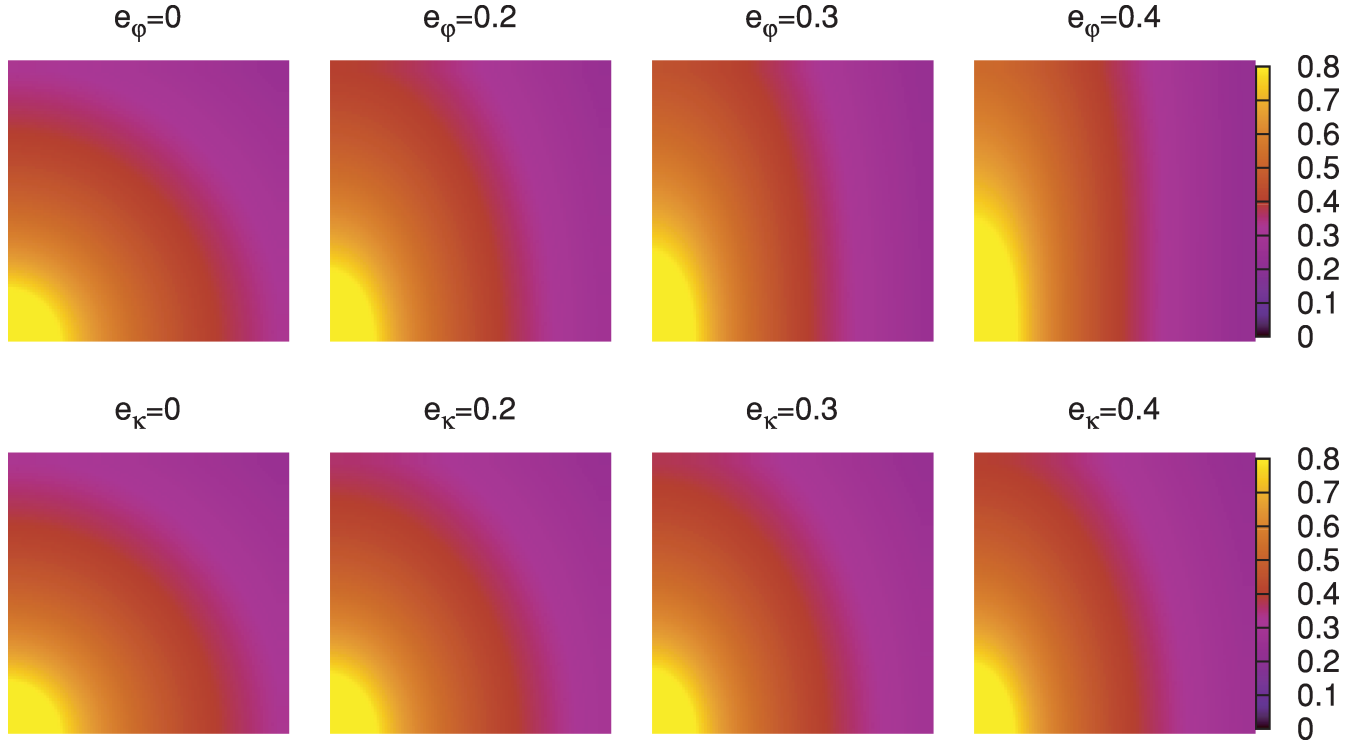
Figure 5. Maps of convergence κ for different values of ellipticity with halo redshift $z_l = 0.5$ and $z_s = 2.0$ and halo mass $M_{\rm vir} = 10^{15}\, h^{-1}\, {\rm M}_\odot$. Ellipticities are again introduced in the *potential* profile (top panels) and in the *density* profile (bottom panels). The field of view is 0.6 arcmin in size.

3.2.2 Elliptical density versus elliptical potential

Simulations typically predict ellipticities in the halo density profile. Therefore, it is interesting to relate the ellipticity introduced in the potential as in the previous section, denoted by e_φ, to the corresponding effective ellipticity in the surface density profile, denoted by e_κ, introduced directly in the convergence map instead of the potential, i.e. by substituting $\theta^2 = \theta_1^2 + \theta_2^2$ in κ by

$$\theta \rightarrow \theta^* = \sqrt{\frac{\theta_1^2}{(1-e_\kappa)} + \theta_2^2 (1-e_\kappa)}\,. \tag{19}$$

In Fig. 5, we show convergence maps for different ellipticities, similarly to Fig. 3. Again, ellipticity e_φ is introduced in the lensing potential (top row) and e_κ in the density (bottom row). Fig. 6 shows a way to relate the two kinds of ellipticity. Enforcing the match $\kappa(\theta_1, \theta_2) = \tilde{\kappa}(\theta^*)$, it shows the relationship between e_κ and e_φ. Here $\kappa(\theta_1, \theta_2)$ is the convergence that results from adding e_φ in the lensing potential and $\tilde{\kappa}$ is the spherically symmetric convergence. Specifically, we match the value of the convergences at the arbitrary matching point $(\theta_1 = 0, \theta_2)$ for various choices of cluster mass, lens and source redshift and matching coordinate θ_2. The relation is quite insensitive to these parameters and also to the value of θ_2 chosen for the match. Overall the relation $e_\varphi = 0.48 e_\kappa$ seems to hold relatively well for $e_\kappa < 0.5$ in the range of parameters considered here. This is consistent with the results of Golse & Kneib (2002) for the extended NFW profile, where they find $e_\kappa \sim 2 e_\varphi$ for $e_\varphi < 0.25$. Our results can be used to relate the typical values of e_κ from simulations to the more convenient values of e_φ used to analytically model the effects of ellipticity.

4 LENSING STATISTICS

4.1 Halo counts

Given the differential comoving number density of lens haloes $dn/d\ln M_{\rm vir}$, one can estimate the cluster number counts dN in the redshift/mass range $dz_l d\ln M_{\rm vir}$ and solid angle $\Delta\Omega$ in the sky as

$$dN(z_l, M_{\rm vir}) = dz_l d\ln M_{\rm vir} \frac{dV(z_l)}{dz_l} \frac{dn(z_l, M_{\rm vir})}{d\ln M_{\rm vir}}\,, \tag{20}$$
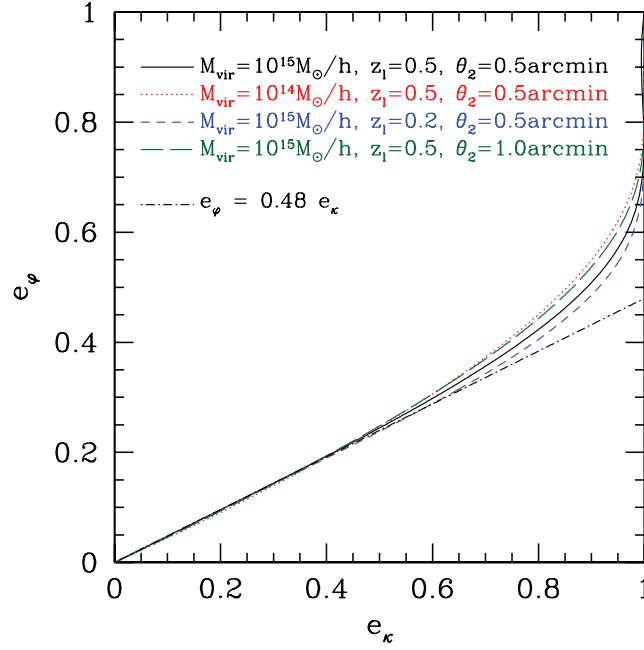
Figure 6. Relationship between e_φ and e_κ which produces the same value of the convergence at the matching point $(\theta_1 = 0, \theta_2)$, shown for different values of halo mass, redshift and matching coordinate θ_2. Because the potential field is smoother than the density field, values of e_φ which are only about half of those of e_κ produce the same convergence field for $e_\kappa < 0.5$.

where $dV/dz_l = \Delta\Omega D_A^2/H$ is the comoving volume element, $D_A(z_l)$ is the comoving angular diameter distance and $H(z_l)$ is the Hubble parameter. The differential halo density n and counts N above a mass threshold M_{th} are given by

$$n(z_l) = \int_{M_{th}}^{\infty} d\ln M_{vir} \frac{dn(z_l, M_{vir})}{d\ln M_{vir}},$$

$$\frac{dN(z_l)}{dz_l} = \Delta\Omega \frac{D_A^2(z_l)}{H(z_l)} n(z_l). \tag{21}$$

4.2 Lensing cross-section

Each halo produces an elliptical 'ring' region around it, with area $\Delta\Omega_\mu(z_l, z_s, M, e_\varphi, \mu_{min})$, such that inside this area the magnification is larger than μ_{min}. This area is an effective cross-section for lensing statistics. Note $\Delta\Omega_\mu$ is the area with $\mu > \mu_{min}$ in the source plane

$$\Delta\Omega_\mu(\mu_{min}) = \int_{\mu > \mu_{min}} d\beta^2 = \int_{\mu(\theta) > \mu_{min}} \frac{d\theta^2}{\mu(\theta)}, \tag{22}$$

where we used the fact that the magnification is precisely the Jacobian of the transformation between image and source coordinates $\mu = d\theta^2/d\beta^2$. A reference value for $\Delta\Omega_\mu$ is the projected cluster surface area defined by its virial radius in the image plane $\Delta\Omega_{vir} = \pi\theta_{vir}^2$. For large values of μ we expect the magnification region to be well inside the halo core and therefore $\Delta\Omega_\mu \ll \Delta\Omega_{vir}$, whereas for $\mu \to 1$, $\Delta\Omega_\mu$ becomes formally infinite. For a given halo, we estimate $\Delta\Omega_\mu$ by evaluating μ in a square grid of 100×100 points with side $2\theta_{vir}$. We then multiply the fraction of grid points with $\mu > \mu_{min}$ by the area $4\theta_{vir}^2$; in this fraction, each point is weighted by $1/\mu(\theta)$ at the grid.

Note that the way we estimate $\Delta\Omega_\mu$ is only strictly accurate if $\Delta\Omega_\mu < 4\theta_{vir}^2$. This is not true for sufficiently low μ, where $\Delta\Omega_\mu$ formally covers the whole sky. In principle, this estimation can be improved by adaptively surveying a radius larger than $2\theta_{vir}$ around the halo. For the goal of estimating the lensing probability, this is not necessary as discussed in the next two sections.

In Fig. 7, we show $\Delta\Omega_\mu$ and $\Delta\Omega_{vir}$ as a function of halo mass, redshift, ellipticity and minimum magnification. Since $r_{vir} \sim M_{vir}^{1/3}$, we have that $\Delta\Omega_{vir} \sim M_{vir}^{2/3}$. For this high value of μ_{min}, $\Delta\Omega_\mu$ is many orders of magnitude smaller but growing faster with M_{vir}. Since $r_{vir} \sim [\Delta_c(z)E^2(z)]^{-1/3}$, we have that $\Delta\Omega_{vir} \sim \Delta_c(z)^{-2/3}E(z)^{-4/3}D_A(z)^{-2}$. The redshift dependence of $\Delta\Omega_{vir}$ is dominated by that of D_A, since $\Delta_c(z)$ and $E(z)$ change less. In particular, it increases rapidly at low redshifts, where $D_A \to 0$. On the other hand $\Delta\Omega_\mu$, which shows a similar trend at intermediate redshifts, goes to zero as $z_l \to 0$ or z_s, where the lensing efficiency vanishes.

As also apparent from the magnification maps, there is a relatively weak dependence on e_φ, where ellipticity mainly distorts the critical curves, but do not change their area. A strong dependence on μ_{min} can be seen; the largest areas come from $\mu_{min} \lesssim 2$ even for the most massive haloes. We will see below that once we sum over halo mass, the contribution of high magnification ($\mu \gtrsim 2$) regions to observable number counts is very small.
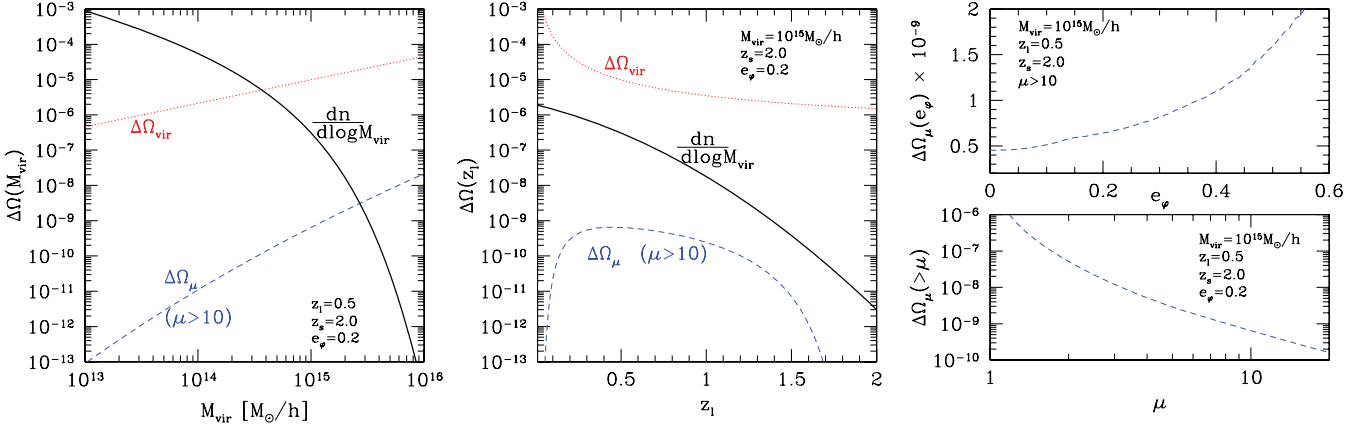
Figure 7. Virial and lensing cross-sections (in rad^2) as a function of halo mass, redshift, ellipticity and minimum magnification. Left: both $\Delta\Omega_\mu$ and $\Delta\Omega_{\rm vir} = \pi\theta_{\rm vir}^2$ as a function of halo mass $M_{\rm vir}$ for $z_l = 0.5$, $z_s = 2.0$, $e_\varphi = 0.2$ and $\mu_{\rm min} = 10$. Middle: same but as a function of z_l for $M_{\rm vir} = 10^{15}\, h^{-1}\, {\rm M}_\odot$. Right: $\Delta\Omega_\mu$ versus e_φ for $\mu_{\rm min} = 10$ (upper panel) and versus μ for $e_\varphi = 0.2$ (lower panel).

4.3 Sky fraction with large magnifications: lensing optical depth

We can estimate the fraction f_μ of the sky with $\mu > \mu_{\rm min}$ due to all haloes above a certain mass and redshift range as

$$f_\mu = \int_0^{z_s} {\rm d}z_l\, \frac{D_A^2(z_l)}{H(z_l)} \int_{M_{\rm th}}^\infty {\rm d}\ln M_{\rm vir} \int_0^\infty {\rm d}z_s\, P(z_s) \int_0^1 {\rm d}e_\varphi\, P(e_\varphi) \Delta\Omega_\mu(z_l, z_s, M_{\rm vir}, e_\varphi, \mu_{\rm min}) \frac{{\rm d}n(z_l, M_{\rm vir})}{{\rm d}\ln M_{\rm vir}}\,, \tag{23}$$

where $P(z_s)$ is the source redshift distribution and $P(e_\varphi)$ is the distribution of halo ellipticities. This quantity is the optical depth for lensing magnification and determines the probability that a given source galaxy/population is magnified by intervening lens haloes. This definition of f_μ accounts for overlapping angular regions, which are counted multiple times in the integrals in mass and redshift. However it neglects multiple lens events, such as multiple images, since only one event is counted per halo. Therefore, strictly speaking, f_μ is the sky area with large magnifications only for $f_\mu \ll 1$, i.e. $\mu \gg 1$, where no such overlappings occur.

Note also that f_μ can be, and in fact is, larger than 1 at regions with $\mu \sim 1$, i.e. such regions cover the sky many times. In fact, even $\Delta\Omega_\mu$ itself for a given cluster can be as large as the whole sky for $\mu \sim 1$. How large f_μ becomes as μ approaches 1 depends on the top value we allow $\Delta\Omega_\mu$ to have, which in our case was set as $4\theta_{\rm vir}^2$ and causes a saturation in f_μ at ~ 27 for $\mu \lesssim 1$. Even though this top cut-off in $\Delta\Omega_\mu$ affects our computation of f_μ for very low values of μ, it does not significantly change the quantity we are really interested in, the lensing probability $P(>\mu)$ described in the next section, which in any case is close to unity for sufficiently large f_μ.

We can also define a fraction $f_{\rm vir}$, similarly to f_μ, replacing $\Delta\Omega_\mu \to \Delta\Omega_{\rm vir}$. It turns out that the area of haloes defined in this way can be larger than the sky area ($f_{\rm vir} > 1$) if one includes haloes of sufficiently low mass. However, those haloes are unable to produce large magnification areas and therefore f_μ remains smaller than 1 for sufficiently large values of $\mu_{\rm min}$.

For fixed source redshift and cluster ellipticity (in which case $P(z_s)$ and $P(e_\varphi)$ are delta functions) we have

$$\frac{{\rm d}f_\mu}{{\rm d}z_l} = \frac{D_A^2(z_l)}{H(z_l)} \int_{M_{\rm th}}^\infty {\rm d}\ln M_{\rm vir} \Delta\Omega_\mu(z_l, M_{\rm vir}, \mu_{\rm min}) \frac{{\rm d}n(z_l, M_{\rm vir})}{{\rm d}\ln M_{\rm vir}}\,, \tag{24}$$

$$\frac{{\rm d}f_{\rm vir}}{{\rm d}z_l} = \frac{D_A^2(z_l)}{H(z_l)} \int_{M_{\rm th}}^\infty {\rm d}\ln M_{\rm vir} \Delta\Omega_{\rm vir}(z_l, M_{\rm vir}) \frac{{\rm d}n(z_l, M_{\rm vir})}{{\rm d}\ln M_{\rm vir}}\,. \tag{25}$$

In Fig. 8 we show the sky fraction ${\rm d}f_{\rm vir}/{\rm d}z_l$ and ${\rm d}f_\mu/{\rm d}z_l$ as a function of z_l for fixed $z_s = 2.0$, $e_\varphi = 0.2$ and $\mu_{\rm min} = 10$. The latter fraction does not change much for $M_{\rm th} < 10^{12}\, h^{-1}\, {\rm M}_\odot$ since these haloes, though numerous, are unable to produce large magnifications. Very massive haloes produce large magnifications but their abundance is exponentially suppressed.

In the left-hand panel of Fig. 9 we show the sky fraction f_μ as a function of $\mu_{\rm min}$ for $M_{\rm th} = 10^{12}\, h^{-1}\, {\rm M}_\odot$, $z_s = 2.0$ (left). The fraction increases sharply as $\mu_{\rm min}$ approaches 1. The curves with different values of e_φ show that for large magnifications, f_μ can be significantly higher for large ellipticities.

4.4 Lensing probability

Given the lensing optical depth f_μ we obtain the lensing probability as

$$P(>\mu) = 1 - e^{-f_\mu}\,. \tag{26}$$

Note that $P(>\mu) \approx f_\mu$ for $f_\mu \ll 1$ or large magnifications, i.e. small optical depths are themselves the lensing probability. On the other hand, $P(>\mu) \to 1$ for $f_\mu \to \infty$ or small magnifications. Our top cut-off value of $4\theta_{\rm vir}^2$ for $\Delta\Omega_\mu$ implied a saturation of $f_\mu \sim 27$ for $\mu \sim 1$. At this value of f_μ, however, $P(>\mu)$ is already very close to unit for all practical purposes and therefore is not significantly affected by the cut-off.
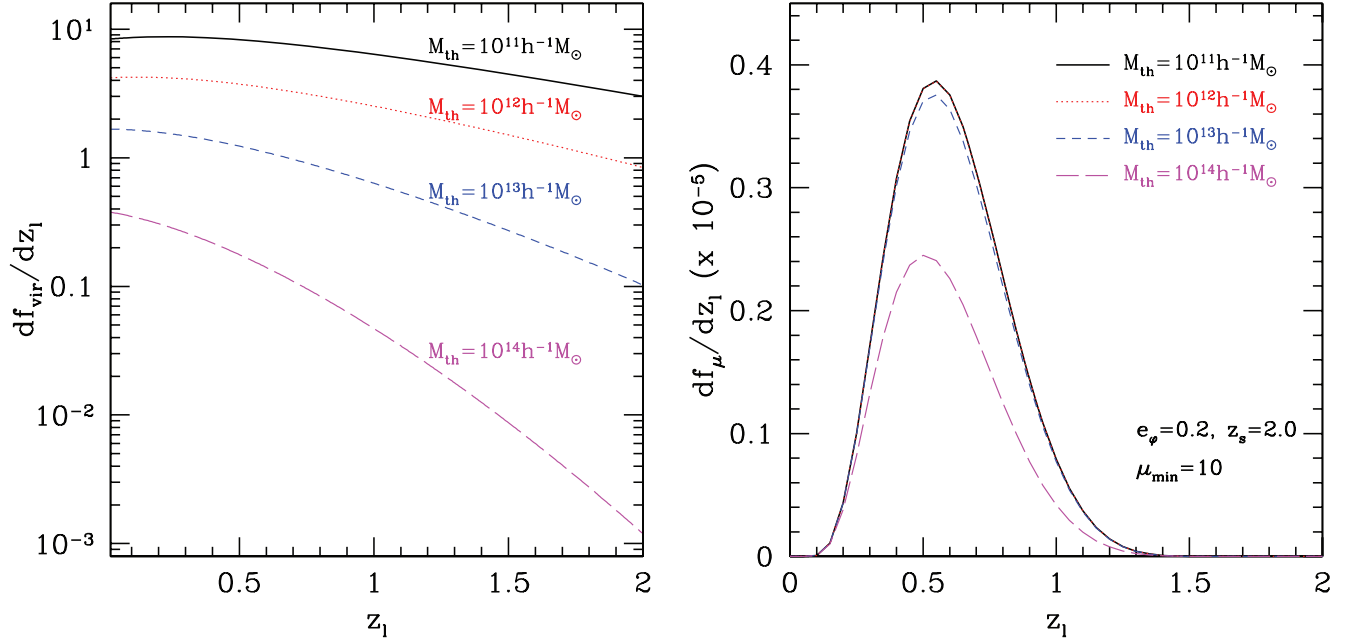
Figure 8. Left: differential sky fraction df_{vir}/dz_l as a function of z_l for haloes above different mass thresholds as indicated. Right: differential sky fraction df_μ/dz_l for haloes with magnification above $\mu_{min} = 10$ and different mass thresholds.
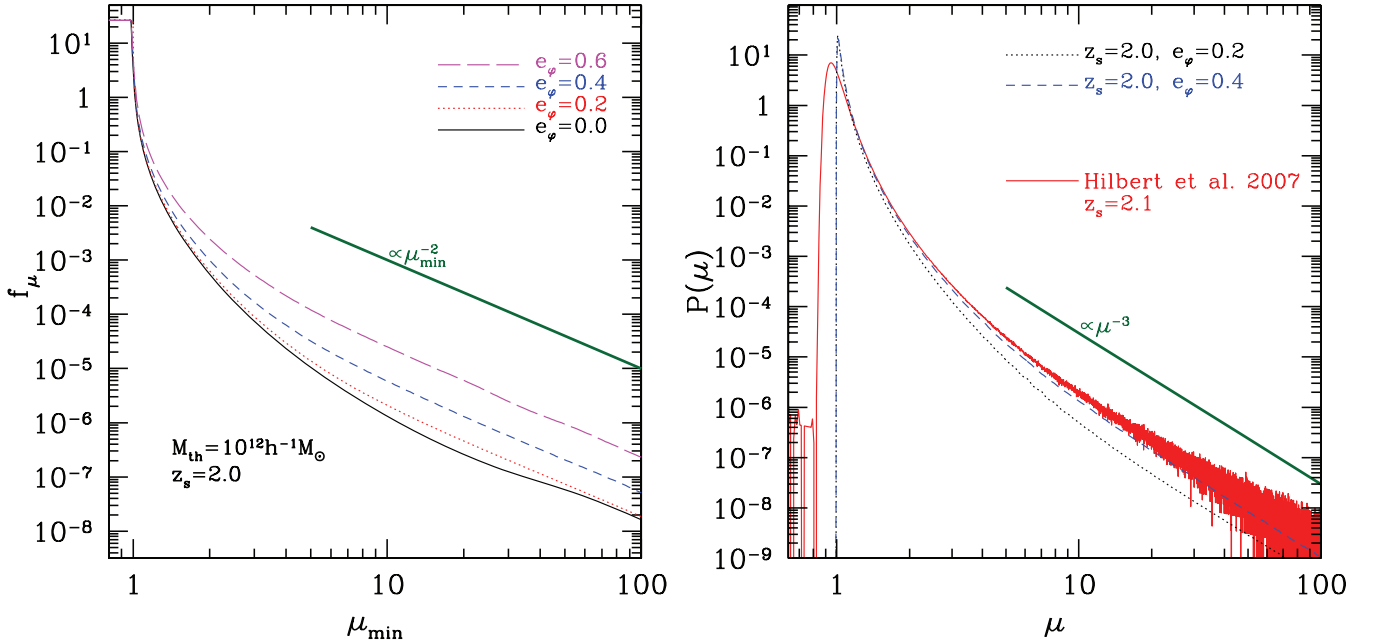

Figure 9. Left: sky fraction f_μ with magnification $\mu > \mu_{min}$ as a function of μ_{min} for haloes with masses $M_{vir} > 10^{12} \, h^{-1} \, M_\odot$ and different ellipticities e_φ. Right: lensing probability $P(\mu)$ to have magnification along the line of sight up to $z_s = 2.0$ from all intervening haloes, assumed to have $e_\varphi = 0.2$ (dotted line) and $e_\varphi = 0.4$ (dashed line). Also shown is the lensing probability obtained from N-body simulations (thin solid line) for sources at $z_s = 2.1$ (Hilbert et al. 2007).

Note $P(>\mu)$ is the probability that a source galaxy is magnified by more than μ and therefore it can be expressed in terms of the probability density $P(\mu)$ as

$$P(>\mu) = \int_\mu^\infty P(\mu) d\mu \,. \tag{27}$$

Alternatively $P(\mu)$ can be obtained by $P(\mu) = -dP(>\mu)/d\mu$. These statistics can then be incorporated in various applications to estimate the effects of lensing magnification. An interesting property of the lensing probability in the source plane is that $P(>\mu) \propto 1/\mu^2$ and therefore $P(\mu) \propto 1/\mu^3$ for $\mu \gg 1$, as can be shown in particular cases and argued to be true in general (Schneider et al. 1992).

In the right-hand panel of Fig. 9, we show $P(\mu)$ for $z_s = 2.0$ and $e_\varphi = 0.2, 0.4$. We also show the magnification probability for sources at $z_s = 2.1$ from Hilbert et al. (2007), obtained by ray-tracing high-resolution *N*-body simulations. Notice that, for $\mu \gg 1$, $P(>\mu) \sim f_\mu \propto \mu^{-2}$ as shown in the left-hand panel of Fig. 9, and it follows that $P(\mu) \propto \mu^{-3}$ as expected. Our semi-analytical estimate of $P(\mu)$ with $e_\varphi = 0.4$ compares relatively well with the probability obtained from ray-tracing on *N*-body simulations (Hilbert et al. 2007; Paciga et al. 2009) at large magnifications.

Even though $e_\varphi = 0.2$ is in better agreement with the average values of halo ellipticities (Jing & Suto 2002), the fact that our model does not include halo substructure and other realistic effects such as other haloes along the line of sight that enhance magnification appears to be incorporated by artificially increasing the halo ellipticity to $e_\varphi = 0.4$. In addition, the semi-analytical model underestimates $P(\mu)$ compared to the simulation results at low magnifications ($\mu \lesssim 1.0$). That is expected since our model only includes a one-halo term and does not properly account for the effects of voids, where highly de-magnified regions sit. That feature is well captured by simulations and can potentially be obtained in an improved version of our model that includes compensated haloes, a two-halo term (Cooray & Sheth 2002) as well as halo substructure (Meneghetti et al. 2007). In our estimations of lensing results on high-redshift galaxy populations, we use $P(\mu)$ from *N*-body simulations (Hilbert et al. 2007).

Finally, note that $P(\mu)$ defined above *averages* over clusters in the line of sight up to the source redshift z_s. When we are interested in the effects within a specific cluster solid angle, we must use only the region around the cluster to define the lensing probability. For instance, if we want to estimate lensing effects within the virial radius of a specific cluster, we use a probability defined simply as $P(>\mu) = \Delta\Omega_\mu / \Delta\Omega_{vir}$, where these quantities are calculated from our semi-analytical model described above.

5 OBSERVABLE EFFECTS OF LENSING MAGNIFICATION

5.1 Counts of submillimetre galaxies

SMGs are dusty galaxies, typically optically obscured but visible in wavelengths below 1 mm due to the thermal spectrum re-emitted by the dust grains after absorbing radiation from the star-forming regions. The simplest prescription for the spectral energy distribution (SED) of SMGs is it is given by a blackbody spectrum B_ν at a high temperature T_{gal}, modified by an emissivity $\epsilon \propto \nu^\beta$

$$S_\nu^{SED} = \epsilon B_\nu \propto \nu^{3+\beta} \left\{ \exp\left[\frac{h\nu}{k_B T_{gal}} \right] - 1 \right\}^{-1} \propto \nu^{3+\beta} \left\{ \exp\left[\frac{(\nu/\text{GHz})}{21(T_{gal}/\text{K})} \right] - 1 \right\}^{-1}. \tag{28}$$

Apart from an overall normalization factor, the two free parameters β and T_{gal} as well as the galaxy redshift z_s must be known. Typical fits to observed galaxies give high redshifts of $z_s \sim 1$–6, values of β in the range 0.5–2 and temperatures of $\sim$15–40 K. Specifically, in our fiducial prescription we assume that all galaxies are at $z_s = 2$ (though we also show some results for $z_s = 3.0$ and 4.0), and take $T_{gal} = 30$ K and $\beta = 0.7$. In the Rayleigh–Jeans regime of low frequencies, the temperature is unimportant and $S_\nu^{SED} \propto \nu^{2+\beta}$. The value of $\beta = 0.7$ is consistent with the spectral index $\alpha = 2 + \beta$ used by Knox et al. (2004) and White & Majumdar (2004). Using the SED prescription one can scale fluxes at one observed frequency ν to another frequency of interest ν', e.g. in the SZ flux range. As we will see, $\beta = 0.7$ properly accounts for extrapolated fluxes in the empirically motivated model of Lagache et al. (2004) for the SED of SMGs at different frequencies.

The count distribution of SMGs have been measured at various wavelengths, including at 250, 350 and 500 μm by Balloon-borne Large Aperture Submillimetre Telescope (BLAST) (Devlin et al. 2009), at 850 μm by Submillimeter Common-User Bolometer Array (SCUBA) (Coppin et al. 2006), at 1100 μm by Millimeter-Wave Bolometer Camera (BOLOCAM) (Laurent et al. 2005) and AzTEC (Perera et al. 2008), and at 1200 μm by Max-Planck Millimeter Bolometer (MAMBO) (Greve et al. 2004). See Pearson & Khan (2009) for a recent compilation of these measurements, a model for fitting them and prospects for future measurements.

In our standard prescription we take the differential counts dn/dS_ν of the SMG population as measured by the BLAST at $\lambda = 500$ μm ($\nu \sim 600$ GHz), and scale various quantities of interest to other frequencies according to the SED prescription. When studying the effects of lensing on the properties of SMGs, we also consider the example of a Schechter model, in which the exponential steepness of the counts make the lensing effects more dramatic.

5.1.1 Magnification and number counts

As a result of photon and energy conservation, the surface brightness of galaxy sources, defined as the flux per unit solid angle, is conserved by gravitational lensing. Since magnification, by definition, increases the solid angle Ω of sources by a factor μ, it has to also increase their intrinsic flux S, effectively lowering the observed threshold and increasing the number of sources available

$$S \to S_{obs} = \mu S, \tag{29}$$

$$d\Omega \to d\Omega_{obs} = \mu d\Omega. \tag{30}$$

As a result, the intrinsic number density of a source population is modified by lensing magnification. For a given magnification μ, the intrinsic differential number density dn/dS is modified as (see e.g. equation 11 in Refregier & Loeb 1997)

$$\frac{dn}{dS} \to \frac{1}{\mu^2} \frac{dn}{dS} \left(\frac{S_{obs}}{\mu} \right). \tag{31}$$

The $1/\mu^2$ factor comes from transforming the angle differential $d\Omega$ (implicit in the above equation) and the flux differential dS into their observed counterparts. The additional change is from the fact that the observed flux S_{obs} corresponds to a true flux of $S = S_{\text{obs}}/\mu$. The intrinsic differential number density can be interpreted as the probability density $P(S)$ of having intrinsic flux S from a random source. Likewise, the observed modified distribution represents the probability density $P(S_{\text{obs}}|\mu)$ of having an observed flux S_{obs} given a magnification μ. In order to obtain the probability $P(S_{\text{obs}})$ of having S_{obs} irrespective of magnification, we must multiply by $P(\mu)$ and integrate over all values of μ.

Given the differential number density, a number of quantities are of interest, such as the cumulative number density, the cumulative number counts $N(>S)$ in a solid angle $\Delta\Omega$, the average total flux of the galaxy population $(\overline{S})^{\text{gal}}$ and its associated Poisson variance $(\overline{S^2})^{\text{gal}}$

$$n(>S) = \int_S \frac{dn}{dS'} dS', \tag{32}$$

$$N(>S) = \Delta\Omega \, n(>S), \tag{33}$$

$$\overline{S} = \Delta\Omega \int S \frac{dn}{dS} dS, \tag{34}$$

$$\overline{S^2} = \Delta\Omega \int S^2 \frac{dn}{dS} dS. \tag{35}$$

Ignoring the clustering of the galaxy population, which adds extra noise to the average flux, the expected fluctuation in the average flux of galaxies within solid angle $\Delta\Omega$ due to Poisson noise in the counts is given by

$$\sigma^{\text{gal}}(S) = \sqrt{\overline{S^2}}. \tag{36}$$

The average flux in one frequency ν can be scaled to ν' given an SED prescription S_ν^{SED}

$$\overline{S}_{\nu'} = \Delta\Omega \int S_{\nu'} \frac{dn}{dS_{\nu'}} dS_{\nu'} \sim \frac{S_{\nu'}^{\text{SED}}}{S_\nu^{\text{SED}}} \Delta\Omega \int S_\nu \frac{dn}{dS_\nu} dS_\nu = \frac{S_{\nu'}^{\text{SED}}}{S_\nu^{\text{SED}}} \overline{S}_\nu, \tag{37}$$

and a similar rescaling can be applied to $\sigma^{\text{gal}}(S_\nu)$. Lensing magnification modifies these various quantities to their observed values according to the effect of a given magnification μ and the lensing probability $P(\mu)$ of actually having that magnification. Since we define $P(\mu)$ in the *source* plane, we may identify angular averages in this plane with averages over $P(\mu)$. For a variable X, we have

$$\frac{1}{\Delta\Omega} \int d\Omega X = \int d\mu P(\mu) X. \tag{38}$$

This implies

$$\langle\mu\rangle = \int d\mu P(\mu)\mu = \frac{\Delta\Omega_{\text{obs}}}{\Delta\Omega}. \tag{39}$$

Using the relation between averages in the observed (image) and intrinsic (source) plane, i.e.

$$\frac{1}{\Delta\Omega_{\text{obs}}} \int d\Omega_{\text{obs}} X = \frac{1}{\langle\mu\rangle\Delta\Omega} \int \mu d\Omega X = \frac{1}{\langle\mu\rangle} \int d\mu \, \mu \, P(\mu) X, \tag{40}$$

and the fact that observations can only average in the image plane, we obtain the observed lensed quantities in terms of their unlensed counterparts

$$\frac{dN_{\text{obs}}(S_{\text{obs}})}{dS_{\text{obs}}} = \frac{1}{\langle\mu\rangle} \int d\mu \frac{P(\mu)}{\mu} \frac{dn}{dS}\left(\frac{S_{\text{obs}}}{\mu}\right), \tag{41}$$

$$N_{\text{obs}}(>S_{\text{obs}}) = \frac{1}{\langle\mu\rangle} \int d\mu P(\mu) n\left(>\frac{S_{\text{obs}}}{\mu}\right), \tag{42}$$

$$N_{\text{obs}}(>S_{\text{obs}}) = \frac{1}{\langle\mu\rangle} \int d\mu P(\mu) N\left(>\frac{S_{\text{obs}}}{\mu}\right), \tag{43}$$

$$\overline{S}_{\text{obs}} = \overline{S}, \tag{44}$$

$$\overline{S^2}_{\text{obs}} = \frac{\langle\mu^2\rangle}{\langle\mu\rangle} \overline{S^2}, \tag{45}$$

where

$$\langle\mu^\alpha\rangle = \int d\mu \, \mu^\alpha P(\mu). \tag{46}$$

When considering the effects of all haloes in the line of sight of source galaxies at large sky patches, we use the $P(\mu)$ defined in Section 4.4. When considering the effect of the source population on a single cluster, we use $P(\mu)$ defined within the cluster radius. Even though an intrinsic solid angle $\Delta\Omega_{\text{int}}$ corresponds to an observed solid angle $\Delta\Omega_{\text{obs}} = \langle\mu\rangle\Delta\Omega_{\text{int}}$, here we assume that the angle implicit in equations (43–45) is simply fixed by the observation, i.e. $\Delta\Omega_{\text{obs}} = \Delta\Omega$, where $\Delta\Omega$ was used to define unlensed quantities equations (33–35). Notice that equation (44) reflects the conservation of total surface brightness by lensing and along with equation (45), is only valid when these quantities are integrated over all fluxes. If we introduce lower or higher limits of integration, we need to integrate over $P(\mu)$ as for the other quantities. In that case equation (44) is no longer true, i.e. the lensed and intrinsic brightness differ.

Paciga et al. (2009) considered the lensing effect on the distribution of SMGs detected at 850 μm. However, they did not include the factors of $1/\langle\mu\rangle$ and $1/\mu$ in the expression for the differential counts equation (41). That caused an overestimation of the magnification effects, which are highly sensitive to the steepness of the differential counts.

If the intrinsic differential number density can be parametrized as a power law with index α *near* the flux threshold,

$$\frac{\mathrm{d}n(S)}{\mathrm{d}S} \propto S^{-\alpha}\,, \tag{47}$$

then the above expressions become simply their intrinsic counterparts rescaled by moments of the magnification probability $P(\mu)$, e.g.

$$\frac{\mathrm{d}N_{\mathrm{obs}}(S_{\mathrm{obs}})}{\mathrm{d}S_{\mathrm{obs}}} = \frac{\langle\mu^{\alpha-1}\rangle}{\langle\mu\rangle}\frac{\mathrm{d}n(S_{\mathrm{obs}})}{\mathrm{d}S}\,, \tag{48}$$

and similarly for $N_{\mathrm{obs}}(>S_{\mathrm{obs}})$ and other observables of interest. Notice that since $P(\mu) \propto 1/\mu^3$ as $\mu \to \infty$, the observed quantities diverge for large enough values of α, unless we impose an upper integration limit defining a maximum magnification or a cut-off in the counts distribution. In practice, there is always a maximum magnification imposed, for instance, by the size of the source galaxies. Moreover, a constant power-law index does not hold for counts over all fluxes. For a non-evolving population in Euclidean flat space $\alpha = 2.5$; larger/smaller values of α indicate a luminosity or density that is increasing/decreasing in time, i.e. non-trivial evolution of the galaxy population.

5.1.2 Number counts from BLAST

In Fig. 10, we illustrate lensing effects on the distribution of SMGs for the BLAST 500 μm data. We show the *measured* BLAST distributions, which we take to be intrinsic as opposed to observed for illustrative purposes. Shown in Fig. 10 are the differential and cumulative number density, as well as the corresponding lensed distributions, assuming sources at different redshifts. We spline interpolate the original BLAST points to obtain a smooth distribution at arbitrary values of flux density.

Obviously, the measured distributions already have lensing effects convolved, which ideally one would try to deconvolve to obtain the true distributions. If the lensing effects are relatively small, as in this case, the above assumption is self-consistent since the observed distribution is in fact already close to the true one. The data indicate that the observed differential counts have an index $\alpha \sim 2$ until $S \sim 10\,\mathrm{mJy}$ and $\alpha \sim 4$ beyond this flux. Note that for $\alpha > 3$ the differential number density increases significantly (see equation 48) and the relative difference between the lensed and unlensed curves increases at the bright end by up to ~ 60 per cent. The empirically motivated model of Lagache et al. (2004) predicts a distribution at 500 μm that is quite close to the one measured by BLAST, suggesting that the observed slopes are already close to the true ones. However, in order for the total brightness inferred from the BLAST points not to exceed the cosmic infrared background (CIB) (Dwek et al. 1998; Fixsen et al. 1998; Smail, Ivison & Blain 1997; Hughes et al. 1998), it is necessary to impose a sharp cut-off flux of $S_{\mathrm{cut}} = 4.6\,\mathrm{mJy}$ (Devlin et al. 2009). In Section 5.1.3, we consider a case that does not require such cut-off, where fluxes decay at the faint end and have much steeper intrinsic slopes at the bright end.

Here, we have integrated up to a maximum magnification of $\mu_{\mathrm{max}} = 100$. However, the results remain nearly the same even for $\mu_{\mathrm{max}} = 10$, reflecting the rarity of high magnification events displayed in Fig. 9. Therefore, our results are insensitive to a magnification cut-off introduced
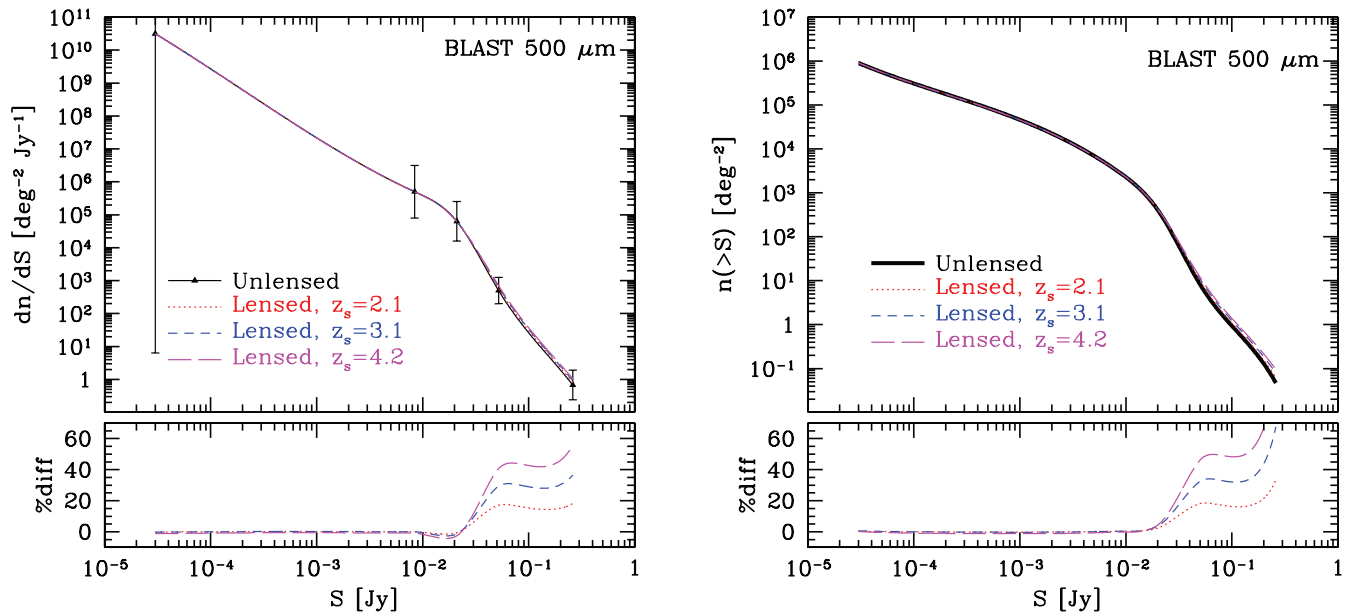

Figure 10. Left: intrinsic differential number density dn/dS from BLAST 500 μm data (points and solid black line) as well as observed lensed counts dN_{obs}/dS_{obs} at different source redshifts (dotted and dashed lines). Here, the observed BLAST data are assumed to be the true underlying distribution at different redshifts, which is then lensed by intervening haloes. Right: cumulative number density for the same unlensed/lensed BLAST distribution.
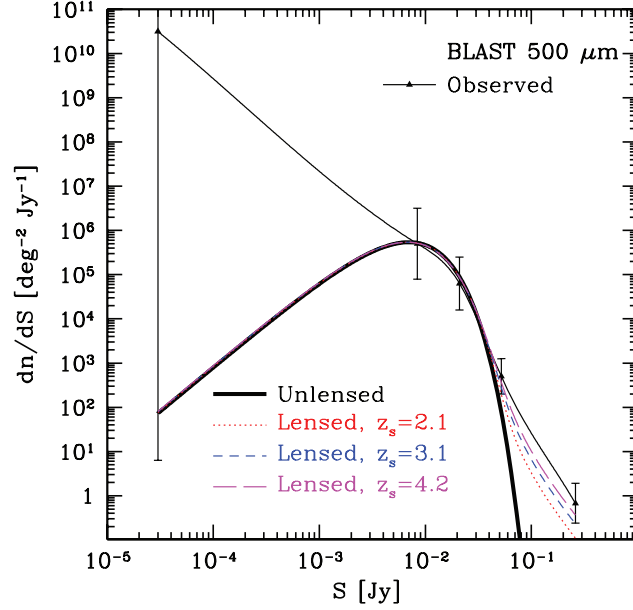
Figure 11. Intrinsic differential density dn/dS from BLAST 500 μm data (points and thin solid line) as well as observed lensed counts dN_{obs}/dS_{obs} at different source redshifts (dotted and dashed lines). Here, the true underlying distribution is assumed to be of a Schechter type (thick solid line), which is then lensed by intervening haloes into the observed BLAST distribution. The underlying distribution fits the middle BLAST points and, when lensed, is roughly consistent with the brightest point.

by finite size of source galaxies (e.g. Takada & Hamana 2003). The actual value of μ_{max} depends on the galaxy population considered and for SMGs is estimated to be $\mu_{max} \sim 10$–30 (Perrotta et al. 2002). However, as discussed in Paciga et al. (2009), there are still large uncertainties on the sizes of SMGs, and there is one SMG lensed by the Abell 2218 cluster, whose magnification is estimated to be $\mu \sim 45$ (Kneib et al. 2004).

5.1.3 Schechter-like distribution

Since the effect of lensing depends on the local slope of the differential counts, we expect much larger magnifications if the intrinsic distribution is sufficiently steep. For illustrative purposes now we assume that the intrinsic counts distribution is of a Schechter type (Schechter 1976)

$$\frac{dn(S)}{dS} = \left(\frac{N}{S'}\right)\left(\frac{S}{S'}\right)^{\gamma} e^{-S/S'}, \tag{49}$$

such that, after lensing, it becomes close to the *measured* BLAST distribution. Beyond the turnaround flux S', this function becomes extremely steep and lensing is very effective. As an example we fix parameter values for this distribution as $\gamma = 2, N = 3.5 \times 10^3, S' = 3.5$ mJy, and show the lensed distributions in Fig. 11. Here, the Schechter function fits intermediate points and decreases fast enough at faint fluxes so as not to exceed the CIB flux. The lensed distribution is consistent with the BLAST data given the error bars if these galaxies are at redshifts $z_s \gtrsim 2$. In this context, observed counts above ~ 40 mJy have all been highly magnified from intrinsic lower fluxes. Note the agreement with the brightest point can be improved at the expense of a larger disagreement with intermediate points by, e.g., increasing the normalization factor N.

In the absence of strong theoretical motivation for the intrinsic distribution, and given the relatively large error bars on the faint end, we did not attempt to fit any particular model to the observed counts. However, given the two extreme cases considered here, it can be seen that the data can be fit by a variety of models, with very different implications for the evolution of the luminosity function of these galaxies.

5.2 SZ mass estimation

The CMB has specific intensity spectrum I_{CMB} of a blackbody with temperature $T_{CMB} \sim 2.725$ K. In terms of $x = h\nu/k_B T_{CMB} = \nu/(56.78\,\text{GHz})$ and $I_0 = 2h/c^2(k_B T_{CMB}/h)^3 = 2.699 \times 10^8$ Jy sr^{-1} we have

$$I_{CMB} = B_\nu = \frac{2h\nu^3}{c^2}(e^{h\nu/k_B T_{CMB}} - 1)^{-1} = \frac{I_0 x^3}{e^x - 1}. \tag{50}$$

As CMB photons cross the cluster hot gas and interact with its high temperature electrons via inverse Compton scattering, the outgoing photons gain energy, shifting their occupation number, temperature and intensity.

The change in specific intensity can be computed by solving the full relativistic Boltzmann equation and expanding in powers of $\theta_e = (k_B T_e/m_e c^2)$ (Itoh et al. 1998) to obtain

$$\frac{\Delta I_\nu}{I_0} = f(x, T_e)g(x)y,\tag{51}$$

where T_e is the electron temperature, $g(x) = x^4 e^x/(e^x - 1)^2$, the Compton y-parameter is defined as

$$y = \sigma_T \theta_e \int n_e dl = \frac{k_B \sigma_T}{m_e c^2} \int n_e(l) T_e(l) dl\tag{52}$$

and $f(x, T_e) = f_0(x) = x(e^x + 1)/(e^x - 1) - 4$, neglecting terms of higher order in θ_e, which are negligible in the non-relativistic regime.

Since $I_\nu = dS_\nu/d\Omega$, the change in flux ΔS_ν through the cluster is computed by integrating over the cluster solid angle $d\Omega = dA/d_A^2$

$$\Delta S_\nu^{SZ} = \int \Delta I_\nu d\Omega = I_0 f(x, T_e)g(x)Y,\tag{53}$$

with the integrated Compton Y-parameter given by

$$Y = \int y d\Omega = \frac{k_B \sigma_T}{m_e c^2} \int n_e T_e dl d\Omega = \frac{1}{d_A^2} \frac{k_B \sigma_T}{m_e c^2} \int n_e T_e dV,\tag{54}$$

and the cluster volume element is $dV = dA dl = d_A^2 d\Omega dl$. One can model electron density n_e and temperature T_e profiles and compute Y from them. Since the total number of electrons in the cluster $N_e = \int n_e dV$ is proportional to the total cluster mass times the gas fraction f_{gas}, one expects the scaling $\int n_e T_e dV \propto M_{gas} T_{gas}$. Further considerations for the case of a gas in virial equilibrium produce the expected scaling relation

$$Y \propto f_{gas}^{5/3} \frac{E(z)^{2/3}}{d_A^2(z)} M^{5/3}.\tag{55}$$

We employ fits from hydrodynamic simulations of Nagai (2006) for this relation given by

$$Y = A_{14} \times 10^{-6} E(z)^{2/3} \left(\frac{h^{-1}\text{Mpc}}{d_A(z)}\right)^2 \left(\frac{M}{10^{14}\, h^{-1}\, M_\odot}\right)^{\alpha_m}.\tag{56}$$

Therefore, given the cluster mass M and redshift z_l we can estimate its integrated Y parameter through the scaling relation, and the change in flux density follows from equation (53).

In our results we consider two mass definitions for the scaling relation. We use parameter values $A_{14} = 2.5, \alpha_m = 5/3$, which are appropriate for the mass M_{vir} defined within the virial radius. These values are roughly intermediate between adiabatic simulations and those with cooling and star formation processes. Similarly, we take $A_{14} = 7.0, \alpha_m = 5/3$, for the mass M_{2500} defined within the radius r_{2500} where the halo overdensity is 2500 times the critical density.

In Fig. 12, we show the blackbody spectrum I_{CMB} as well as the SZ distortion for haloes at $z_l = 0.5$ and with different virial masses. Here, we employed the non-relativistic limit $f(x, T_e) = f_0(x)$ for illustrative purposes.
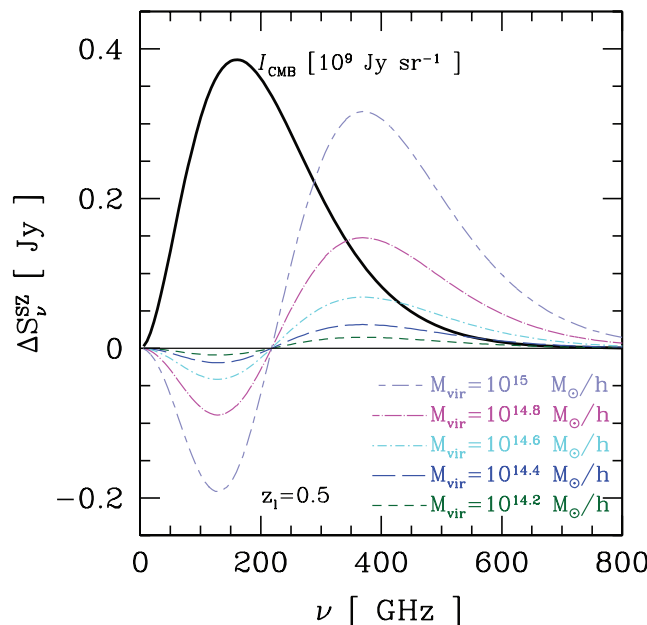

Figure 12. Blackbody intensity I_{CMB} (thick solid line) and SZ flux densities ΔS_ν^{SZ} for haloes at $z_l = 0.5$ and virial masses ranging from $10^{14.2}$ to 10^{15} h^{-1} M$_\odot$ (dashed and dot–dashed lines).

5.2.1 Contamination of the SZ signal

We now estimate the effect of SMGs and their magnification on the SZ signal of clusters. SMGs have typical spectra that peak at $\sim 100\,\mu$m, but they still have significant flux around ~ 1 mm, where the SZ effect becomes important.

Since the SZ effect is measured by subtracting the flux of the CMB photons in the line-of-sight of the halo from the average flux of background CMB photons, adding an average flux $\overline{S}_\nu$ from background galaxies in principle does not affect the signal, since the background is removed by the subtraction. This remains true even with lensing since the average flux does not change (equation 44). However, local flux fluctuations $\sigma^{\mathrm{gal}}(S_\nu)$ in the background flux due to Poisson noise in galaxy counts cannot be removed.

The true SZ flux $\Delta S_\nu^{\mathrm{SZ}}$ is then modified by $\sigma^{\mathrm{gal}}(S_\nu)$. These fluctuations are further increased by lensing magnification to $\sigma_{\mathrm{obs}}^{\mathrm{gal}}(S_\nu)$ so that the 68 per cent range of the observed SZ flux becomes

$$\left(\Delta S_\nu^{\mathrm{SZ}} \right)_{\mathrm{obs}} = \Delta S_\nu^{\mathrm{SZ}} \pm \sigma_{\mathrm{obs}}^{\mathrm{gal}}(S_\nu). \tag{57}$$

In the absence of lensing effects the flux noise is simply $\sigma_{\mathrm{obs}}^{\mathrm{gal}}(S_\nu) = \sigma^{\mathrm{gal}}(S_\nu) = \sqrt{\overline{S^2}_\nu}$ where the fluctuation is within the cluster virial radius

$$\overline{S^2}_\nu = \Delta\Omega_{\mathrm{vir}} \int \mathrm{d}S_\nu S_\nu^2 \frac{\mathrm{d}n}{\mathrm{d}S_\nu} \,. \tag{58}$$

In Fig. 13, we show the SZ flux for clusters of various masses at $z_{\mathrm{l}} = 0.5$ and the contributions of background SMGs. Here the average flux and its noise are computed with the BLAST distribution at $\lambda = 500\,\mu$m ($\nu = 600$ GHz) and extrapolated to other frequencies using the SED prescription. The average background flux $\overline{S}_\nu$ from these galaxies within the virial radius of the cluster is rather significant: it is larger than the SZ signal. However, as a 'background' it can be subtracted. Without lensing, the noise $\sigma^{\mathrm{gal}}(S_\nu)$ in the flux is substantially smaller than the background, but non-negligible in comparison to the SZ signal.

For clusters of large mass, even though the fluctuations from background galaxies increase due to the larger cluster area, these fluctuations become a smaller fraction of the total SZ signal, and relatively less important. Less massive clusters, however, are highly affected by the fluctuations of SMGs. For clusters of mass $10^{14.6}\,h^{-1}\,\mathrm{M}_\odot$, expected to be above the minimum mass detected by upcoming surveys, even the unlensed contamination is comparable to the SZ increment. The right-hand panels of Fig. 13 show the effect of using a different aperture in the definition of mass and SMG contamination. Note the relative level of contamination remains about the same without lensing.

In both panels, magnification due to the cluster is rather significant, especially in the case of SZ fluxes through smaller radii (r_{2500}), since those are confined to cluster cores of high magnification. The flux noise is magnified by factors of ~ 2–7. Magnification due to large-scale structure in the line of sight is much smaller – it enhances the noise by only a few per cent.

The left-hand panel of Fig. 14 shows results for clusters of virial mass $10^{14.6}\,h^{-1}\,\mathrm{M}_\odot$, but with the Lagache model for the flux from SMGs (Lagache et al. 2004). As mentioned earlier, the Lagache model agrees well with the BLAST data at $\lambda = 500\,\mu$m, so the dotted and dashed lines are nearly identical to those of the middle left panel of Fig. 13. For the Lagache model, the count distributions are available at
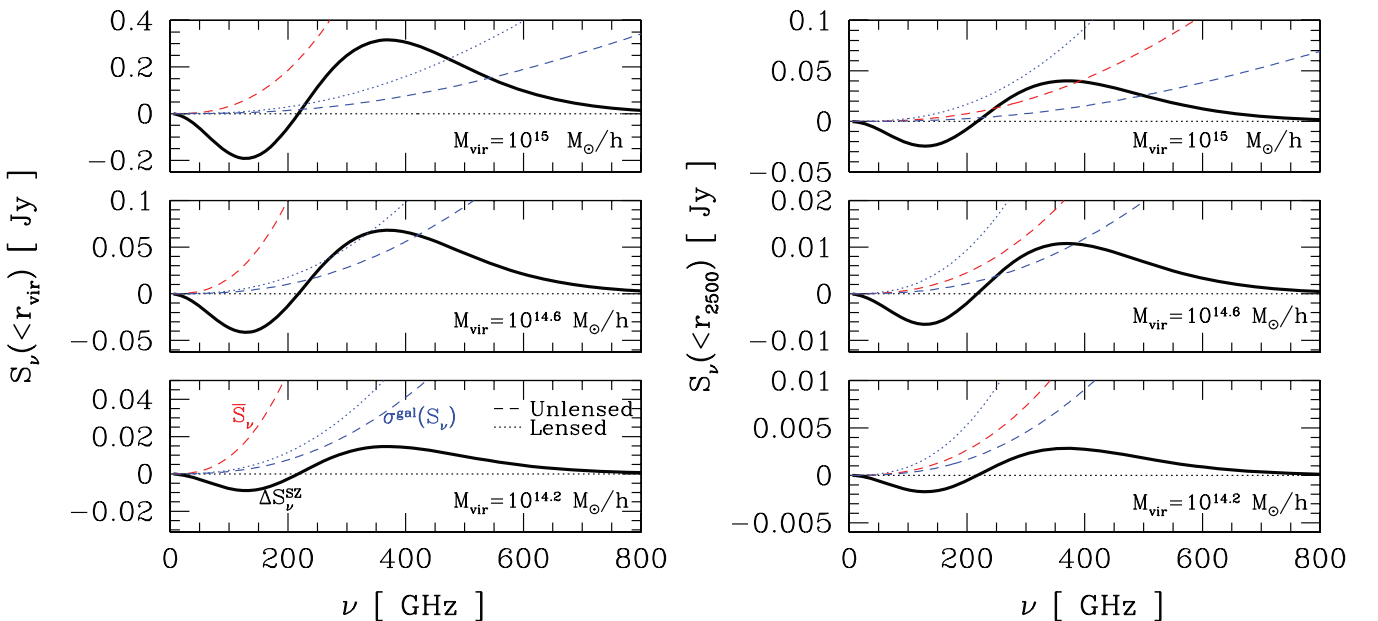

Figure 13. SZ flux for clusters of different masses at $z_{\mathrm{l}} = 0.5$ (solid thick line) and the corresponding average background flux $\overline{S}_\nu$ and noise $\sigma^{\mathrm{gal}}(S_\nu)$ within the cluster radius from a population of SMGs at $z_{\mathrm{s}} = 2.0$ (dashed lines). Left: fluxes measured within the virial radius r_{vir}. Right: fluxes measured within r_{2500}. Radii and masses are converted with the prescription of Hu & Kravtsov (2003) for an NFW profile. For clusters of larger masses, the fluctuations from background galaxies increase, but become a smaller fraction of the total SZ signal. Lensing magnification (dotted lines) further enhances the flux noise, especially within smaller apertures.
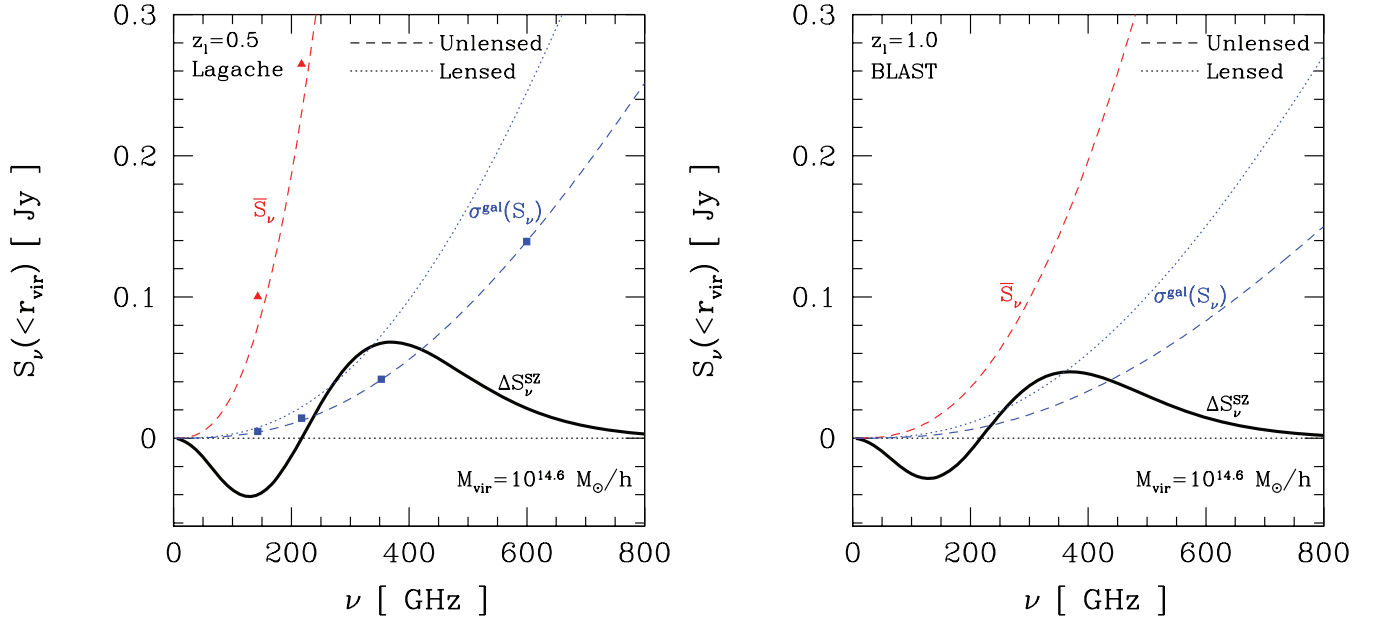
Figure 14. SZ flux for clusters with a virial mass of $10^{14.6}\,h^{-1}\,M_\odot$, as in the middle-left panel of Fig. 13. Left: instead of using the BLAST data, we employ the Lagache model for estimating contamination by SMGs. The dashed and dotted lines are still computed extrapolating from the $\nu = 600\,\mathrm{GHz}$ value with the SED prescription. Triangle and square dots denote average fluxes and Poisson fluctuations at exact wavelengths $\lambda = 500, 850, 1380, 2097\,\mu\mathrm{m}$, and show that the extrapolation agrees well with the model. Right: same as middle-left panel of Fig. 13, but for cluster redshift $z_l = 1.0$. Both $\Delta S_\nu^{\mathrm{SZ}}$ and the contribution of SMGs decrease for higher z_l, but the contamination level remains roughly the same.

wavelengths within the SZ range. The triangle and square dots shown here are computed directly from the Lagache model at $\lambda = 500, 850, 1380, 2097\,\mu\mathrm{m}$ ($\nu = 600, 350, 220, 140\,\mathrm{GHz}$). Note that the SED extrapolation from $\lambda = 500\,\mu\mathrm{m}$ (dotted and dashed lines) fits well the model points.

The right-hand panel of Fig. 14 shows the results for the BLAST data, but for a cluster redshift of $z_l = 1.0$. The qualitative results again do not change. We have verified this for other masses and redshifts as well.

6 CONCLUSION

We have implemented a halo model calculation of magnification effects of galaxy and cluster haloes. We explored the reliability of our model and compared it with published results from simulations. The one-halo term computed in the model describes well the magnification probability at large magnifications, but underestimates it at regions of de-magnification ($\mu < 1$). The effects of compensating haloes and addition of a two-halo term (Cooray & Sheth 2002), as well as the effects of cluster substructure, can further improve our semi-analytical calculation.

We applied magnification probability distributions from numerical simulations (Hilbert et al. 2007) to the counts of distant galaxies. Our results differ from those of Paciga et al. (2009): our expression differs from theirs by two magnification factors, leading to a significantly smaller lensing contribution than their estimate. For the counts of high-redshift SMGs recently observed, we find that lensing leads to enhancements of at least 60 per cent at the bright (steep) end of the counts. In particular cluster fields with large magnification cross-section, this enhancement can be significantly larger.

Galaxy cluster surveys that utilize the SZ effect are susceptible to at least three kinds of contamination: by radio galaxies associated with the cluster, by high-redshift SMGs that lie behind the cluster and by projection effects due to large-scale structure. The latter may result, for instance, from additional groups and clusters below the survey detection threshold which end up being projected on observed clusters (Hallman et al. 2007). Here, we estimated the contribution of SMGs over the frequency range targeted by SZ surveys. We used the counts from the BLAST survey, extrapolated to lower frequencies, and included the effects of lensing magnification from simulations and semi-analytical estimates.

We find that for clusters with masses between 10^{14} and 10^{15} solar masses, there is a significant contamination from SMGs at frequencies higher than the SZ null at 220 GHz. This contribution arises from the irreducible variance of the Poisson distribution of the SMGs. It is comparable to the SZ excess at 350 GHz at the low-mass end, and is about half the SZ excess for a mass of $M_{\mathrm{vir}} = 4 \times 10^{14}$ solar masses (it can be either an excess or a deficit for a particular cluster). With arcmin-sized beams, SMGs are confusion limited, so it is not possible to isolate and remove their contribution. These results are consistent with earlier studies of the (unlensed) contribution estimated from SCUBA sources (White & Majumdar 2004). We also find that lensing from the cluster cores significantly enhances this irreducible noise, especially for SZ fluxes within small apertures containing the cluster critical curves.

Our results imply that SZ surveys must model the contamination noise of SMGs at the SZ null and for channels at higher frequencies. The value of the signal measured in such channels is significantly contaminated, even for the highest mass clusters due to lensing magnification. At frequencies below the SZ null, the SMG contribution is at the few per cent level for mass ranges of interest. So it is less likely to be a problem in cluster detection in the SZ decrement regime, but must be included for cosmological measurements, as even a few per cent bias in the inferred cluster mass can affect derived cosmological parameters due to the steepness of the mass function (especially at the high mass end).

ACKNOWLEDGMENTS

REFERENCES

Barger A. J., Cowie L. L., Sanders D. B., Fulton E., Taniguchi Y., Sato Y., Kawara K., Okuda H., 1998, Nat, 394, 248
Bartelmann M., Schneider P., 2001, Phys. Rep., 340, 291
Birkinshaw M., 1999, Phys. Rep., 310, 97
Blain A. W., 1996, MNRAS, 283, 1340
Blain A. W., 1997, MNRAS, 290, 553
Blain A. W., 1999, MNRAS, 304, 669
Blain A. W., Longair M. S., 1993, MNRAS, 264, 509
Blain A. W., Smail I., Ivison R. J., Kneib J.-P., Frayer D. T., 2002, Phys. Rep., 369, 111
Blandford R. D., Narayan R., 1992, ARA&A, 30, 311
Bryan G. L., Norman M. L., 1998, ApJ, 495, 80
Bullock J. S., Kolatt T. S., Sigad Y., Somerville R. S., Kravtsov A. V., Klypin A. A., Primack J. R., Dekel A., 2001, MNRAS, 321, 559
Carlstrom J. E., Holder G. P., Reese E. D., 2002, ARA&A, 40, 643
Cooray A., Sheth R., 2002, Phys. Rep., 372, 1
Coppin K. et al., 2006, MNRAS, 372, 1621
Devlin M. J. et al., 2009, Nat, 458, 737
Diego J. M., Partridge B., 2009, preprint (arXiv:0907.0233)
Diego J. M., Tegmark M., Protopapas P., Sandvik H. B., 2007, MNRAS, 375, 958
Dwek E. et al., 1998, ApJ, 508, 106
Fixsen D. J., Dwek E., Mather J. C., Bennett C. L., Shafer R. A., 1998, ApJ, 508, 123
Golse G., Kneib J.-P., 2002, A&A, 390, 821
Greve T. R., Ivison R. J., Bertoldi F., Stevens J. A., Dunlop J. S., Lutz D., Carilli C. L., 2004, MNRAS, 354, 779
Haiman Z., Mohr J. J., Holder G. P., 2001, ApJ, 553, 545
Hallman E. J., OShea B. W., Burns J. O., Nornman M. L., Harkness R., Wagner R., 2007, ApJ, 671, 27
Hilbert S., White S. D. M., Hartlap J., Schneider P., 2007, MNRAS, 382, 121
Hoekstra H., Jain B., 2008, Annu. Rev. Nuclear-Part. Sci., 58, 99
Hu W., 2003, Phys. Rev. D, 67, 081304
Hu W., Kravtsov A. V., 2003, ApJ, 584, 702
Hughes D. H. et al., 1998, Nat, 394, 241
Itoh N., Kohyama Y., Nozawa S., 1998, ApJ, 502, 7
Jing Y. P., Suto Y., 2002, ApJ, 574, 538
Kneib J., van der Werf P. P., Kraiberg Knudsen K., Smail I., Blain A., Frayer D., Barnard V., Ivison R., 2004, MNRAS, 349, 1211
Knox L., Holder G. P., Church S. E., 2004, ApJ, 612, 96
Lagache G. et al., 2004, ApJS, 154, 112
Laurent G. T. et al., 2005, ApJ, 623, 742
Lima M., Hu W., 2005, Phys. Rev. D, 72, 043006
Lima M., Hu W., 2007, Phys. Rev. D, 76, 123013
Meneghetti M., Bartelmann M., Moscardini L., 2003, MNRAS, 340, 105
Meneghetti M., Bartelmann M., Jenkins A., Frenk C., 2007, MNRAS, 381, 171
Nagai D., 2006, ApJ, 650, 538
Narayan R., Bartelmann M., 1996, preprint (arXiv:9606001)
Navarro J. F., Frenk C. S., White S. D. M., 1997, ApJ, 490, 493
Paciga G., Scott D., Chapin E. L., 2009, MNRAS, 395, 1153
Pearson C. P., Khan S. A., 2009, MNRAS, 399, L11
Perera T. A. et al., 2008, MNRAS, 391, 1227
Perrotta F., Baccigalupi C., Bartelmann M., De Zotti G., Granato G. L., 2002, MNRAS, 329, 445
Refregier A., Loeb A., 1997, ApJ, 478, 476
Rozo E., Wechsler R. H., Koester B. P., Evrard A. E., McKay T. A., 2007, preprint (arXiv:0703574)
Rozo E. et al., 2010, ApJ, 708, 645
Schechter P., 1976, ApJ, 203, 297

Schneider P., Ehlers J., Falco E. E., 1992, Gravitational Lenses. Springer-Verlag, Berlin

Schneider P., Kochanek C. S., Wambsganss J., 2006, Gravitational Lensing: Strong, Weak and Micro. Springer-Verlag, Berlin

Scott D., White M., 1999, A&A, 346, 1

Sheth R. K., Tormen G., 1999, MNRAS, 308, 119

Smail I., Ivison R. J., Blain A. W., 1997, ApJ, 490, L5

Spergel D. N. et al., 2003, ApJS, 148, 175

Sunyaev R. A., Zeldovich Y. B., 1972, Comments Astrophys. Space Phys., 4, 173

Takada M., Hamana T., 2003, MNRAS, 346, 949

Takada M., Jain B., 2003a, MNRAS, 340, 580

Takada M., Jain B., 2003b, MNRAS, 344, 857

Wang L., Steinhardt P. J., 1998, ApJ, 508, 483

White M., 2001, A&A, 367, 27

White M., Majumdar S., 2004, ApJ, 602, 565

APPENDIX A: LENSING BY ELLIPSOIDAL HALOES

The effects of lensing on source images are introduced in Section 3.1. It is useful here to recall basic results for the axially symmetric lens case before considering the elliptical case. In general, the deflection angle vector $\boldsymbol{\alpha} = (\alpha_1, \alpha_2)$ relating source and image angles can be obtained from the convergence field $\kappa(\theta)$ by

$$\boldsymbol{\alpha}(\boldsymbol{\theta}) = \frac{1}{\pi} \int d^2\theta' \kappa(\theta') \frac{\boldsymbol{\theta} - \boldsymbol{\theta'}}{|\theta - \theta'|^2} \,, \tag{A1}$$

where $\boldsymbol{\theta} = (\theta_1, \theta_2)$. If the density profile has axial symmetry, so do all statistical quantities derived from it. In particular the lensing potential is independent of the position angle with respect to the lens centre $\varphi(\theta_1, \theta_2) = \varphi(\theta)$. Choosing the lens centre as the origin of the coordinate system, the deflection vector points towards the lens centre with magnitude

$$\alpha(\theta) = \frac{1}{\pi\theta} \int 2\pi\theta' d\theta' \kappa(\theta') = \frac{m(\theta)}{\theta} \,, \tag{A2}$$

where $m(\theta) = M(<\theta)/\pi D_l^2 \Sigma_{\text{crit}}$ with $M(<\theta)$ being the mass within θ.

Given an axially symmetric lensing potential $\varphi(\theta)$, we obtain the elliptical generalization with major axis along the θ_2-direction by replacing $\theta^2 = \theta_1^2 + \theta_2^2$ by

$$\theta \to \bar{\theta} = \sqrt{\frac{\theta_1^2}{(1 - e_\varphi)} + \theta_2^2(1 - e_\varphi)} \,. \tag{A3}$$

Using the derivatives $\partial\bar{\theta}/\partial\theta_1$ and $\partial\bar{\theta}/\partial\theta_2$, the Cartesian components of the deflection angle are given by

$$\alpha_1 = \frac{\partial\varphi}{\partial\theta_1} = \frac{\theta_1}{(1 - e_\varphi)\bar{\theta}} \tilde{\alpha}(\bar{\theta}) \,,$$

$$\alpha_2 = \frac{\partial\varphi}{\partial\theta_2} = \frac{\theta_2(1 - e_\varphi)}{\bar{\theta}} \tilde{\alpha}(\bar{\theta}) \,, \tag{A4}$$

and their derivatives are

$$\frac{\partial\alpha_1}{\partial\theta_1} = \frac{\tilde{\alpha}(\bar{\theta})}{(1 - e_\varphi)\bar{\theta}} + \frac{\theta_1^2}{(1 - e_\varphi)^2\bar{\theta}^2} \left(-\frac{\tilde{\alpha}(\bar{\theta})}{\bar{\theta}} + \frac{d\tilde{\alpha}(\bar{\theta})}{d\bar{\theta}} \right) \,,$$

$$\frac{\partial\alpha_2}{\partial\theta_2} = \frac{\tilde{\alpha}(\bar{\theta})(1 - e_\varphi)}{\bar{\theta}} + \frac{\theta_2^2(1 - e_\varphi)^2}{\bar{\theta}^2} \left(-\frac{\tilde{\alpha}(\bar{\theta})}{\bar{\theta}} + \frac{d\tilde{\alpha}(\bar{\theta})}{d\bar{\theta}} \right) \,,$$

$$\frac{\partial\alpha_1}{\partial\theta_2} = \frac{\partial\alpha_2}{\partial\theta_1} = \frac{\theta_1\theta_2}{\bar{\theta}^2} \left(-\frac{\tilde{\alpha}(\bar{\theta})}{\bar{\theta}} + \frac{d\tilde{\alpha}(\bar{\theta})}{d\bar{\theta}} \right) \,. \tag{A5}$$

Here and below, tildes denote spherically symmetric quantities, e.g. $\tilde{\alpha}(\bar{\theta}) = d\varphi/d\bar{\theta}$. First, let us check the axially symmetric case by setting $e_\varphi = 0$, in which case $\bar{\theta}^2 = \theta^2 = \theta_1^2 + \theta_2^2$ and

$$\frac{\partial\tilde{\alpha}_i}{\partial\theta_j} = \delta_{ij}\frac{\tilde{\alpha}(\bar{\theta})}{\bar{\theta}} + \frac{\theta_i\theta_j}{\bar{\theta}^2} \left(-\frac{\tilde{\alpha}(\bar{\theta})}{\bar{\theta}} + \frac{d\tilde{\alpha}(\bar{\theta})}{d\bar{\theta}} \right) \,. \tag{A6}$$

In this case, the convergence and shear simplify to

$$\tilde{\kappa} = \frac{1}{2} \left(\frac{\tilde{\alpha}(\bar{\theta})}{\bar{\theta}} + \frac{d\tilde{\alpha}(\bar{\theta})}{d\bar{\theta}} \right) \,,$$

$$\tilde{\gamma}_1 = \frac{\theta_1^2 - \theta_2^2}{2\bar{\theta}^2} \left(-\frac{\tilde{\alpha}(\bar{\theta})}{\bar{\theta}} + \frac{d\tilde{\alpha}(\bar{\theta})}{d\bar{\theta}} \right) \,, \quad \tilde{\gamma}_2 = \frac{\theta_1\theta_2}{\bar{\theta}^2} \left(-\frac{\tilde{\alpha}(\bar{\theta})}{\bar{\theta}} + \frac{d\tilde{\alpha}(\bar{\theta})}{d\bar{\theta}} \right) \,,$$

$$|\tilde{\gamma}| = -\frac{1}{2} \left(-\frac{\tilde{\alpha}(\bar{\theta})}{\bar{\theta}} + \frac{d\tilde{\alpha}(\bar{\theta})}{d\bar{\theta}} \right) \,. \tag{A7}$$

Notice that the average value of $\tilde{\kappa}$ within $\bar{\theta}$ is

$$\bar{\kappa}(\bar{\theta}) = \frac{1}{\pi\bar{\theta}^2} \int_0^{\bar{\theta}} 2\pi\theta'\tilde{\kappa}(\theta')\mathrm{d}\theta' = \frac{\tilde{\alpha}(\bar{\theta})}{\bar{\theta}}, \tag{A8}$$

and therefore it is easy to verify the fact that

$$|\tilde{\gamma}| = \frac{1}{2}\left(\frac{\tilde{\alpha}(\bar{\theta})}{\bar{\theta}} - \frac{\mathrm{d}\tilde{\alpha}(\bar{\theta})}{\mathrm{d}\bar{\theta}}\right) = \bar{\kappa} - \tilde{\kappa}. \tag{A9}$$

Using the following equalities

$$\frac{\tilde{\alpha}(\bar{\theta})}{\bar{\theta}} = \tilde{\kappa} + |\tilde{\gamma}|,$$

$$\left(-\frac{\tilde{\alpha}(\bar{\theta})}{\bar{\theta}} + \frac{\mathrm{d}\tilde{\alpha}(\bar{\theta})}{\mathrm{d}\bar{\theta}}\right) = -2|\tilde{\gamma}|, \tag{A10}$$

in the expressions for general ellipticity equations (A5) we obtain

$$\frac{\partial\alpha_1}{\partial\theta_1} = \frac{\tilde{\kappa} + |\tilde{\gamma}|}{(1 - e_\varphi)} - 2|\gamma|\frac{\theta_1^2}{(1 - e_\varphi)^2\bar{\theta}^2},$$

$$\frac{\partial\alpha_2}{\partial\theta_2} = (\tilde{\kappa} + |\tilde{\gamma}|)(1 - e_\varphi) - 2|\gamma|\frac{\theta_2^2(1 - e_\varphi)^2}{\bar{\theta}^2},$$

$$\frac{\partial\alpha_1}{\partial\theta_2} = \frac{\partial\alpha_2}{\partial\theta_1} = -2|\tilde{\gamma}|\frac{\theta_1\theta_2}{\bar{\theta}^2}.$$

Therefore, the convergence is given by

$$\kappa = A(e_\varphi)\tilde{\kappa}(\bar{\theta}) + B(e_\varphi, \theta_1, \theta_2)|\tilde{\gamma}(\bar{\theta})|, \tag{A11}$$

where

$$A(e_\varphi) = \frac{1 + (1 - e_\varphi)^2}{2(1 - e_\varphi)}, \quad B(e_\varphi, \theta_1, \theta_2) = A(e_\varphi) - \frac{\theta_1^2 + \theta_2^2(1 - e_\varphi)^4}{\bar{\theta}^2(1 - e_\varphi)^2}$$

and the shear components are given by

$$\gamma_1 = C(e_\varphi)\tilde{\kappa}(\bar{\theta}) + D(e_\varphi, \theta_1, \theta_2)|\tilde{\gamma}(\bar{\theta})|, \tag{A12}$$

where

$$C(e_\varphi) = \frac{1 - (1 - e_\varphi)^2}{2(1 - e_\varphi)}, \quad D(e_\varphi, \theta_1, \theta_2) = C(e_\varphi) - \frac{\theta_1^2 - \theta_2^2(1 - e_\varphi)^4}{\bar{\theta}^2(1 - e_\varphi)^2}$$

and

$$\gamma_2 = -\frac{2\theta_1\theta_2}{\bar{\theta}^2}|\tilde{\gamma}(\bar{\theta})|. \tag{A13}$$

Therefore, we can compute κ and γ_1 and γ_2, at positions θ_1, θ_2 from the values of $\tilde{\kappa}$ and $|\tilde{\gamma}|$ at $\bar{\theta}$ from the spherical case. The calculation of $|\gamma|$ and μ then follows.

APPENDIX B: HALO MASS CONVERSIONS

Simulations of the SZ effect usually predict its flux decrement/increment for different cluster mass definitions. Observationally, it may be desirable to define SZ halo masses at small apertures (large overdensities), since those can provide fluxes with larger signal-to-noise ratios. Moreover, one expects smaller radii to enclose less flux from radio sources and SMGs (though less SZ signal as well). However, as we show, smaller apertures also correspond to increased flux fluctuations from lensing. We follow the mass conversion recipe outlined in White (2001) and Hu & Kravtsov (2003), which we briefly review here for overdensities defined in terms of the *critical* density.

Converting different halo mass definitions requires assuming a prescription for the halo profile. Throughout, we have been assuming the NFW profile (Navarro et al. 1997)

$$\rho(r) = \frac{\rho_\mathrm{s}}{(r/r_\mathrm{s})(1 + r/r_\mathrm{s})^2}. \tag{B1}$$

For this profile, the mass M_h within radius r_h enclosing an overdensity Δ_h with respect to the *critical* density ρ_c is

$$M_h \equiv \frac{4\pi r_h^3}{3}\Delta_h\rho_\mathrm{c} = 4\pi\rho_\mathrm{s}r_h^3 f(r_\mathrm{s}/r_h), \tag{B2}$$

where the first equality is a definition, the second results from the NFW profile and

$$f(x) = x^3[\ln(1 + x^{-1}) - (1 + x)^{-1}]. \tag{B3}$$

For the usually employed virial mass M_vir the general equation above becomes

$$M_\mathrm{vir} \equiv \frac{4\pi r_\mathrm{vir}^3}{3}\Delta_\mathrm{c}\rho_\mathrm{c} = 4\pi\rho_\mathrm{s}r_\mathrm{vir}^3 f(1/c), \tag{B4}$$

where $c = r_{\rm vir}/r_{\rm s}$ is the halo concentration. From these equations, we can relate M_h to $M_{\rm vir}$ as

$$\frac{M_h}{M_{\rm vir}} = \frac{\Delta_h}{\Delta_{\rm c}} \frac{1}{(cx)^3} \,, \tag{B5}$$

$$x = \frac{r_{\rm s}}{r_h} = f^{-1}\left(\frac{\Delta_h}{\Delta_{\rm c}} f(1/c)\right) \,. \tag{B6}$$

We employ the fitting formula for inversion of $x(f) = f^{-1}$ (Hu & Kravtsov 2003)

$$x(f) = \left[a_1 f^{2p} + \left(\frac{3}{4}\right)^2\right]^{-1/2} + 2f \,, \tag{B7}$$

where $p = a_2 + a_3 \ln f + a_4 (\ln f)^2$ and $(a_1, \ldots, a_4) = (0.5116, -0.4283, -3.13 \times 10^{-3}, -3.52 \times 10^{-5})$. This fit is accurate to better than 1 per cent for the range of virial masses and concentrations used here.

This paper has been typeset from a TeX/LaTeX file prepared by the author.